Multifidelity modeling similarity conditions for airfoil dynamic stall prediction with manifold mapping

Vishal Raul and Leifur Leifsson*

Department of Aerospace Engineering, Iowa State University,

Ames, Iowa, 50011, USA

Structured Abstract

Purpose

The purpose of this work is to investigate the similarity requirements for the application of multifidelity modeling (MFM) for the prediction of airfoil dynamic stall using computational fluid dynamics (CFD) simulations.

Design/methodology/approach

Dynamic stall is modeled using the unsteady Reynolds-averaged Navier-Stokes equations and Menter's shear stress transport turbulence model. Multifidelity models are created by varying the spatial and temporal discretizations. The effectiveness of the MFM method depends on the similarity between the high- (HF) and low-fidelity (LF) models. Their similarity is tested by computing the prediction error with respect to the HF model evaluations. The proposed approach is demonstrated on three airfoil shapes under deep dynamic stall at a Mach number 0.1 and Reynolds number 135,000.

Findings

The results show that varying the trust-region (TR) radius (λ) significantly affects the prediction accuracy of the MFM. The HF and LF simulation models hold similarity within small ($\lambda \leq 0.12$) to medium ($0.12 \leq \lambda \leq 0.23$) TR radii producing a prediction error less than 5%, whereas for large TR radii ($0.23 \leq \lambda \leq 0.41$), the similarity is strongly affected by the time discretization and minimally by the spatial discretization.

Originality/value

The findings of this work present new knowledge for the construction of accurate MFMs for dynamic stall performance prediction using LF model spatial- and temporal discretization setup

^{*}Corresponding author (leifur@iastate.edu)

and the TR radius size. The approach used in this work is general and can be used for other unsteady applications involving CFD-based MFM and optimization.

Keywords: Dynamic stall, unsteady CFD, surrogate modeling, multifidelity modeling, manifold mapping, multifidelity model similarity conditions.

Nomenclature

- Angle of attack, (deg) α
- Mean angle of attack, (deg) α_m
- Ē Favre mean of the flow variable
- Airfoil trailing-edge wedge angle, (deg) β_{TE}
- Kronecker delta δ_{ij}
- Gain ratio γ
- λ Trust-region radius
- Low-fidelity model output c
- f High-fidelity model output
- S Correction matrix
- S Multifidelity model
- Vector of design variables X
- Vector containing lower bounds on design variables \mathbf{x}_{lb}
- Je, (deg) Vector containing upper bounds on design variables \mathbf{x}_{ub}
- Turbulent eddy viscosity, (Pa·s) μ_t
- Pitch rate, (rad/s) ω
- Viscous stress tensor component, (Pa) τ_{ij}
- θ_{TE} Airfoil trailing-edge directional angle, (deg)

- Amplitude of oscillations, (deg) \boldsymbol{A}
- a^s PARSEC surface coefficient
- Chord length, (-) c
- Sectional drag coefficient, (-) c_d

$$= \frac{d}{\frac{1}{2}\rho_{\infty}U_{\infty}^2S}$$

Sectional lift coefficient, (-) c_l

$$= \frac{l}{\frac{1}{2}\rho_{\infty}U_{\infty}^2}$$

Sectional pitching moment coefficient, (-) c_m

$$= \frac{m}{\frac{1}{2}\rho_{\infty}U_{\infty}^2Sc}$$

- Estimated error in average drag coefficient, (d.c.) $c_{d_{err}}$
- Richardson extrapolation estimate of average drag coefficient per cycle, (d.c.) $c_{d_{Est}}$
- dDrag force, (N)
- dtTime step, (sec)
- Scalar objective function f
- Favre fluctuating component of the flow variable
- Inequality constraint function g
- HTotal enthalpy per unit mass, (J/kg)
- hEquality constraint function
- Turbulent kinetic energy, (m²/s²) k
- k_r Reduced frequency

$$= \tfrac{\omega c}{2U_\infty}$$

- l Lift force, (N)
- LAirfoil lower surface
- Pitching moment, (Nm) m

- Static pressure, (Pa) p
- Airfoil leading edge radius R_{LE}
- Reynolds number Re
- S Reference area, (m²)
- time, (sec) t
- Airfoil trailing-edge offset t_{off}
- Airfoil trailing-edge thickness t_{TE}
- Velocity component in Cartesian system, (m/s) и
- U Airfoil upper surface
- Free-stream velocity, (m/s) U_{∞}
- XAirfoil surface crest x-coordinate
- x_c Non-dimensional chordwise location
- y^+ Non-dimensionalized first layer cell thickness
- ZAirfoil surface crest z-coordinate
- z-coordinate of airfoil section z
- Z_{xx} Second order derivative of airfoil surface
- d.c. Drag counts, $\Delta c_d = 0.0001$

Introduction

The predominant features of dynamic stall on aerodynamic surfaces, such as airfoils, wings, and rotor blades, are the formation, generation, and shedding of an energetic leading-edge vortex (LEV) or a dynamic stall vortex (DSV) (McCroskey et al. 1976). These dynamic stall characteristics can induce a nonlinear fluctuating pressure field that produces significant transient variations in the aerodynamic forces and moments that are much larger than their corresponding static magnitudes (Gerontakos & Lee 2006). The transient variations can adversely affect the structural strength, and fatigue life of the

aerodynamic system (Carr 1988, Mani et al. 2012, Wang et al. 2015, Lee & Gerontakos 2004). Rotorcraft and commercial-grade wind turbines (Butterfield 1988, Butterfield et al. 1991, Butterfield 1989) are high Reynolds number applications where the dynamic stall effects are important. At low Reynolds numbers, dynamic stall is observed in vertical axis wind turbines (VAWTs) (Buchner et al. 2015, Wang et al. 2010), and bio-inspired micro air vehicles (MAVs)/unmanned air vehicles (UAVs) (Ellington 1999, Ellington et al. 1996, Van Den Berg & Ellington 1997, Andro & Jacquin 2009, Hu et al. 2018).

Considering the wide field of applications, significant research has been conducted on how to suppress, delay, or eliminate dynamic stall effects using active-passive systems (Yu et al. 1995, Zhao & Zhao 2015, Lee & Gerontakos 2006, Müller-Vahl et al. 2016, Gardner 2016). Aerodynamic shape optimization (ASO) can be used for passive suppression of the dynamic stall effects but poses some significant challenges (Mani et al. 2012, Raul & Leifsson 2021, Wang et al. 2015). In the past, ASO for dynamic stall suppression or delay has received limited attention due to the significant computational cost involved with the optimization process corresponding to costly and repetitive design evaluations, the large number of design variables, and their respective gradient calculations. Nevertheless, there is a growing interest among researchers to produce an ASO strategy to alleviate the dynamic stall problem.

Gradient-based optimization (GBO), a local search approach, is commonly used for ASO. Recently, Wang et al. (Wang et al. 2015, Wang & Zhao 2018) alleviated the dynamic stall characteristics on rotor airfoil by using sequential quadratic programming (SQP). A more efficient GBO approach using the adjoint-based method (Jameson 2003) is also implemented for ASO-based dynamic stall mitigation (Wong et al. 2006, Nadarajah & Jameson 2007, Mani et al. 2012, Economon et al. 2015), mainly due to the efficient computation of gradients and its ability to handle high-dimensional optimization problems (Laurenceau & Meaux 10th April 2008). However, this method has a one major drawback. In particular, the objective function generated from computational simulations is often non-differentiable, discontinuous, and inherently noisy, which makes sensitivity information often inaccessible (Koziel & Yang 2011). Additionally, the adjoint method is dependent on the high-fidelity (HF) simulation model and can be computationally expensive to use for complex unsteady problems.

Surrogate-based optimization (SBO) (Koziel & Yang 2011, Fernández-Godino et al. 2016) has been suggested to alleviate the computational cost of ASO by shifting the computational burden from the time-consuming HF simulation to a fast surrogate model constructed by sparsely sampling the design space. Surrogate models are typically constructed using data-fit methods, such as polynomial regression (Zhou et al. 2005), kriging (Simpson et al. 2001), radial basis functions (RBF) (Forrester et al. 2008), and support vector regression (Forrester et al. 2008). Kriging (Kumar & Cesnik 2015, Tang et al. 2017, Vu & Lee 2015) has been used for performance improvement of rotors with ASO while RBF is more preferred in turbomachinery design (Khalfallah et al. 2015) where the computational cost per design evaluation is similar to dynamic stall cases. Additionally, Kriging regression model has been used for delaying and mitigating dynamic stall characteristics over VAWT airfoil with ASO (Raul & Leifsson 2021).

Construction of an accurate data-fit surrogate model usually requires multiple model evaluations where the cost quickly grows with an increasing number of the design variables, rendering the datafit SBO approach computationally expensive (Fernández-Godino et al. 2016) and time-consuming. Another way to reduce the computational cost is to use multifidelity modeling (MFM) (Peherstorfer et al. 2018). MFM methods combine data from accurate HF simulations and fast low-fidelity (LF) simulations providing better generalization capabilities than single-fidelity data-fit surrogates, leading to an overall reduction in the computational cost. Some of the most widely used multifidelity techniques are cokriging (Forrester et al. 2008), space mapping (Koziel et al. 2008), and manifold mapping (MM) (Echeverría & Hemker 2008, Echeverría et al. 2007). In spite of its success in cost reduction in CFD-based ASO, MFM has received limited attention for dynamic stall mitigation applications. The generation of LF models are critical to MFM and can be generated using various methods such as coarse discretization and simplified physics (Fernández-Godino et al. 2016).

The focus of this work is on the application of MM (Echeverría et al. 2007) to the performance prediction of dynamic stall. In MM, the objective function is constructed from fast but inaccurate LF model evaluations and corrected with HF evaluations over the entire optimization process to construct a local surrogate model that produces fast and accurate HF approximations. In the past, the MM method has been used in various research areas. For example, Hemker et al. (Hemker & Echeverría 2007) introduced the trust-region strategy for MM modeling and used it to optimize a die-press and Thelen et al. (Thelen et al. 2020) used the MM technique for aeroelastic flutter prediction. Blom et al. (Blom et al. 2015) used the MM technique to accelerate the convergence of coupling iterations in fluid-structure interaction problems. MM has not been applied before to the prediction of dynamic stall.

Strong similarity of the HF and LF simulation models is fundamental to the success of optimal design with MFM methods. Similarity is defined here to be how well the multifidelity model outputs follow each other with respect to changes in the input parameters. For example, if the HF model predicts an increase in the output for a given change in the input, the LF model should also predict an increase, although that change many not be of the same magnitude as for the HF model. Furthermore, if the HF and LF predict opposite changes in the output for a given parameter change the similarity condition is violated. Currently, there are no rigorous methods available that provide guidance for the selection of the LF model setup to maintain HF-LF model similarity. An improper selection of the LF model and trust-region radius could make the optimization process inefficient resulting in longer convergence with multiple HF evaluations and the possibility of acquiring spurious optimum designs as well as the failure of the optimization process.

The objective of this work is to investigate the similarity conditions needed for the HF and LF simulation models for accurate prediction of dynamic stall. In particular, a local MFM model is constructed with the MM method to predict the performance metric of an aerodynamic surface under dynamic stall. The approach is investigated using the unsteady Reynolds-averaged Navier-Stokes (URANS) equations and Menter's shear stress transport (SST) turbulence model (Menter 1994) with fine and coarse discretizations as the HF and LF simulation models, respectively. Multiple local MM models are generated using a combination of the HF model and different LF model configurations. Several LF models are generated by selecting varying combinations of the spatial and temporal discretizations. The local MM models are then used to evaluate the dynamic stall of airfoil shapes with small perturbations in several trust-region radii. The prediction accuracy of the MM model is measured by computing prediction error against the HF model dynamic stall prediction and used to determine the similarity between HF and LF models.

The remainder of the paper is organized as follows. In the next section, dynamic stall test case, performance metric and the MFM technique used in this work are described. Following that, the computational fluid dynamics (CFD) model setup, HF model validation, and LF model configuration are described. Then, the results of measuring the performance of the MFM are presented. Finally, the conclusions and suggestions for future work are presented.

Multifidelity modeling

This section describes the dynamic stall test case under consideration, dynamic stall performance metric, and multifidelity modeling and optimization using manifold mapping.

2.1 Dynamic stall test case

The dynamic stall phenomenon is generally studied with a sinusoidally oscillating airfoil in a uniform freestream flow (Fig. 1). The oscillating motion of the airfoil is described using the angle of attack as a

Table 1: Dynamic stall motion and flow parameters (Lee & Gerontakos 2004)

Parameters	Values	Units
α_m	10°	deg
A	15°	deg
ω	3.403	rad/s
k_r	0.05	-
Re	135,000	-

function of time given as

$$\alpha(t) = \alpha_m + Asin(\omega t), \tag{1}$$

where α_m , A, and ω represent the mean angle of attack, the amplitude of the oscillation and the rotational rate, respectively. The reduced frequency, k, is another important parameter relating time unit t of rotation to the time scale of the flow passing over an airfoil section and is defined as

$$k_r = \frac{\omega c}{2U_{\infty}},\tag{2}$$

where c is the chord length and U_{∞} is the freestream speed.

For this study, the deep dynamic stall case from the experimental work conducted by Lee and Gerontakos (Lee & Gerontakos 2004) is considered for validation purposes. Lee and Gerontakos (Lee & Gerontakos 2004) performed wind tunnel experiments to investigate the behavior of an unsteady boundary layer and stall events on the NACA 0012 airfoil with various oscillating motion parameters and reduced frequencies at a Reynolds number of 135,000. The test was conducted in a 0.9 m ×1.2 m ×2.7 m low-speed, suction-type wind tunnel facility with a turbulence intensity of 0.08% at a freestream speed of 35 m/s. The details of flow and motion parameter of the deep dynamic stall case considered in this work are given in Table 1.

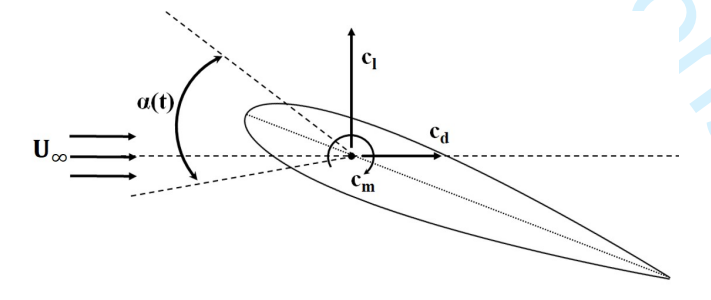


Figure 1: Forces and moments acting on airfoil undergoing a sinusoidal pitching motion about the quarter chord point.

2.2 Dynamic stall performance metric

One of the objective of this work is to build accurate MFM that could predict dynamics stall performance metric of various airfoil shapes which can be in future utilized for ASO based dynamic stall mitigation.

ASO for mitigating dynamic stall characteristics can be defined such that the design variable vector **x** describes the airfoil shape and the objective function defines a performance metric that captures the phenomenon to mitigate and delay the dynamic stall. Such an objective function can be achieved by delaying the DSV development, which is responsible for the abrupt change in aerodynamic loads. Drag and pitching moments are especially sensitive to the occurrence of a DSV on the airfoil surface, which can lead to a sudden divergence in the drag and pitching moment coefficients (Raul & Leifsson 2021). The objective function used in the current study is developed to mitigate this divergence and is written as

$$f(\mathbf{x}) = \left(\frac{\sum_{i=1}^{N} c_{d_i}(\mathbf{x})}{f(c_{d0})}\right) + \left(\frac{\sum_{i=1}^{N} |c_{m_i}(\mathbf{x})|}{f(c_{m0})}\right),\tag{3}$$

where $f(c_{d0}) = \sum_{i=1}^{N} (c_{d0})_i$, $f(c_{m_0}) = \sum_{i=1}^{N} |(c_{m0})_i|$, and $c_d(\mathbf{x})$, and $c_m(\mathbf{x})$ represent the time variant drag coefficient and pitching moment coefficient during dynamic stall cycle, respectively. N is the total number of physical time steps in the dynamic stall simulation. The subscript '0' in the above formulation denotes baseline airfoil parameters. The primary focus of this work is to delay and mitigate the dynamic stall characteristics. Therefore, only the upstroke part of oscillation cycle is considered where the predominant effects of DSV are observed.

As mentioned above, the design variable vector \mathbf{x} describes the airfoil shape. This study uses the PARSEC airfoil parameterization technique (Sobieczky 1999), which offers design variables that are directly related to the airfoil shape, such as the thickness, leading-edge radius, and the trailing-edge wedge angle. The PARSEC technique describes the upper and lower surface of an airfoil as a linear combination of sixth-order shape function as

$$z_s = \sum_{i=0}^{6} a_i^s x_c^{i-\frac{1}{2}}, \quad s = U, L$$
 (4)

where z_s is the z coordinate of airfoil surface, x_c is the chordwise location ($0 \le x_c \le 1$) and a_i are undetermined coefficients. The subscript s refers to the upper (U) or lower (L) surfaces of the airfoil. The PARSEC technique defines the shape of an airfoil of a unit chord length using a total of 12 variables (Fig. 2). The details of the variables are given in Table 2. These variables, along with the chordwise locations and the shape function (4), results in a system of six equations that can be solved to determine

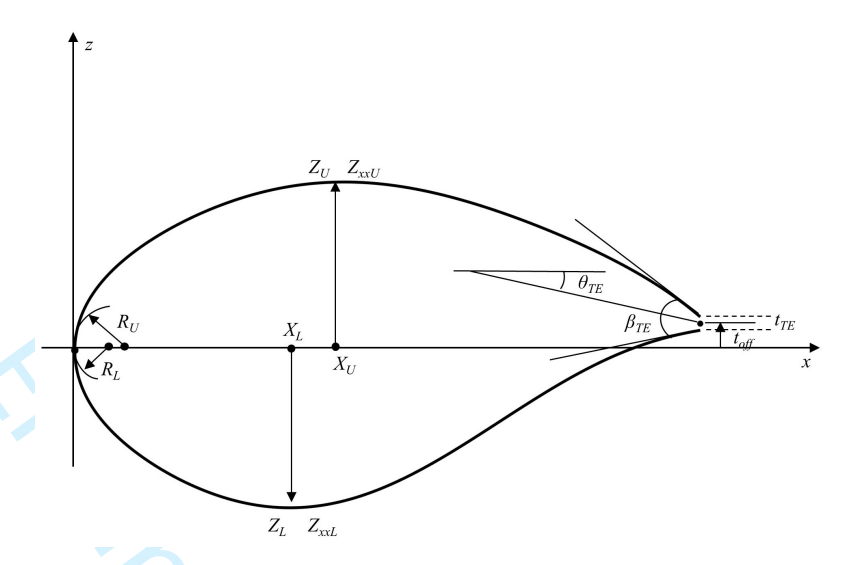


Figure 2: PARSEC airfoil geometry parameters.

Table 2: The PARSEC design variables

Design	Description	Units
Variables		
X	Surface crest x coordinate	-
Z	Surface crest z coordinate	-
Z_{xx}	Second order derivative at X, $\frac{d^2z}{dx^2} _{x=X}$	-
R_{LE}	Leading edge radius	-
$ heta_{TE}$	Trailing-edge directional angle	deg
$oldsymbol{eta}_{TE}$	Trailing-edge wedge angle	deg
t_{off}	Trailing-edge offset	-
t_{TE}	Trailing-edge thickness	-

the six a_i^s coefficients for each airfoil surface (Leifsson & Koziel 2015). Since the formation of the DSV is strongly affected by the leading-edge radius and the upper airfoil surface, only variables affecting the upper surface are considered to reduce the dimensionality of the problem along with a common variable R_{LE} representing a leading-edge radius such that $R_{LE} = R_U = R_L$. The variables defining the lower surface are set to be the same as for the baseline airfoil (the NACA 0012 in this work). Additionally, the trailing-edge thickness (t_{TE}) and trailing-edge offset (t_{off}) are set to zero, which generates airfoil shapes with sharp trailing-edges and with the trailing-edge point at (0,1). These changes reduce the current problem dimensions from twelve to six with the design variable vector now written as

$$\mathbf{x} = [X_U, Z_U, Z_{xx_U}, R_{LE}, \theta_{TE_U}, \beta_{TE_U}]^T.$$
 (5)

Table 2 defines the design variables and Table 3 gives their bounds. These bounds are selected to allow for large perturbations of the shape without producing atypical airfoil shapes.

Table 3: Design variable bounds representing airfoil upper surface

Design Variables	Upper bound	Lower bound	Units
	\mathbf{x}_{ub}	\mathbf{x}_{lb}	
$\overline{X_U}$	0.5011	0.2733	-
Z_U	0.09	0.054	-
Z_{xx_U}	-0.4036	-0.6726	-
R_{LE}	0.0222	0.0104	-
$ heta_{TE_U}$	-7.0294	-11.7156	deg
eta_{TE_U}	5.8803	3.52818	deg

2.3 Manifold mapping

Multifidelity modeling (Peherstorfer et al. 2018) is a method to construct a fast and accurate model using data from high- and low-fidelity physics-based simulations. The high-fidelity (HF) model evaluates the system under consideration at the desired accuracy, whereas the low-fidelity (LF) model provides a fast evaluation of the same metric but at a lower accuracy than the high-fidelity one.

In this work, the manifold mapping (MM) (Echeverría et al. 2007, Echeverría & Hemker 2008) technique is used to construct the multifidelity model, $\mathbf{s}(\mathbf{x})$, that corrects the misalignment between high-fidelity, $\mathbf{f}(\mathbf{x})$, and low-fidelity, $\mathbf{c}(\mathbf{x})$, models. This correction is obtained by generating a mapping $\mathbf{s}(\mathbf{x})$ where the response $\mathbf{c}(\mathbf{x}_f^*)$ is mapped to $\mathbf{f}(\mathbf{x}_f^*)$, where \mathbf{x}_f^* is the optimum design point, and the tangent plane for $\mathbf{c}(\mathbf{x})$ at \mathbf{x}_f^* is mapped to the tangent plane for $\mathbf{f}(\mathbf{x})$ at \mathbf{x}_f^* . The affine mapping $\mathbf{s}(\mathbf{x})$ is defined as (Echeverría et al. 2007)

$$\mathbf{s}(\mathbf{x}) = \mathbf{f}(\mathbf{x}_f^*) + \mathbf{S}(\mathbf{c}(\mathbf{x}) - \mathbf{c}(\mathbf{x}_f^*)),$$

$$\mathbf{S} = \mathbf{J}_f(\mathbf{x}_f^*) \, \mathbf{J}_c^{\dagger}(\mathbf{x}_f^*).$$
(6)

where

$$\mathbf{S} = \mathbf{J}_f(\mathbf{x}_f^*) \, \mathbf{J}_c^{\dagger}(\mathbf{x}_f^*). \tag{7}$$

Here, $\mathbf{J}_f(\mathbf{x}_f^*)$ is the Jacobian of the high-fidelity model at \mathbf{x}_f^* and $\mathbf{J}_c(\mathbf{x}_f^*)$ is Jacobian for the low-fidelity model at \mathbf{x}_f^* , and the pseudo-inverse is indicated with the symbol \dagger .

The mapping $\mathbf{s}(\mathbf{x})$ is a local surrogate for the high-fidelity model and can be used with an optimizer as

$$\mathbf{x}_{\mathrm{mm}}^* = \arg\min_{\mathbf{x}} \ \mathbf{s}(\mathbf{x}),\tag{8}$$

where \boldsymbol{x}_{mm}^{*} is a local optimum of the high-fidelity model. The convergence to the local optimum requires the generation of the multifidelity model at each iteration for which the correction matrix S needs to be updated. The computation of the correction matrix S requires gradient information for the Jacobian matrix. Thus, the MM model is defined at each iteration i as

$$\mathbf{s}^{(i)}(\mathbf{x}) = \mathbf{f}(\mathbf{x}^{(i)}) + \mathbf{S}^{(i)}(\mathbf{c}(\mathbf{x}) - \mathbf{c}(\mathbf{x}^{(i)})). \tag{9}$$

In this work, the gradients are challenging to compute. Hence, an approximation to the correction matrix is used. In particular, the correction matrix $\mathbf{S}^{(i)}$ at iteration i is computed as (Echeverría et al. 2007)

$$\mathbf{S}^{(i)} = \begin{cases} \Delta \mathbf{F} \cdot \Delta \mathbf{C}^{\dagger} & \text{when } i > 0 \\ \mathbf{I} & \text{otherwise} \end{cases}$$
 (10)

where

$$\Delta \mathbf{F} = \left[\mathbf{f}(\mathbf{x}^{(i)}) - \mathbf{f}(\mathbf{x}^{(i-1)}) \quad \dots \quad \mathbf{f}(\mathbf{x}^{(i)}) - \mathbf{f}(\mathbf{x}^{\max(i-n,0)}) \right], \tag{11}$$

and

$$\Delta \mathbf{C} = \left[\mathbf{c}(\mathbf{x}^{(i)}) - \mathbf{c}(\mathbf{x}^{(i-1)}) \quad \dots \quad \mathbf{c}(\mathbf{x}^{(i)}) - \mathbf{c}(\mathbf{x}^{\max(i-n,0)}) \right], \tag{12}$$

where n denotes dimensionality of the design space. This correction ensures that $\mathbf{s}^{(i)}(\mathbf{x})$ is consistent with $\mathbf{f}(\mathbf{x}^{(i)})$ at all high-fidelity samples. The matrix $\Delta \mathbf{C}^{\dagger}$ is the pseudoinverse of the matrix $\Delta \mathbf{C}$ and written as

$$\Delta \mathbf{C}^{\dagger} = \mathbf{V}_{\Delta \mathbf{C}} \mathbf{\Sigma}_{\Delta \mathbf{C}}^{\dagger} \mathbf{U}_{\Delta \mathbf{C}}^{T}, \tag{13}$$

where $V_{\Delta C}$, $\Sigma_{\Delta C}$ and $U_{\Delta C}$ are obtained by single value decomposition (SVD) of the matrix ΔC . The matrix $\Sigma_{\Delta C}^{\dagger}$ is computed by inverting the nonzero entries in $\Sigma_{\Delta C}$ and keeping the zero entries unchanged.

The MM method is typically employed within a trust-region (Du et al. 2019) based optimization framework (Alexandrov et al. 1998), where in every iteration the objective function is optimized using the MM model in the current trust-region. As the optimization continues to the HF optimum, the MM model is corrected based on all the gathered data. It should be noted that the MM modeling technique can be efficiently used without the availability of exact gradient information (Du et al. 2019), and still has shown to converge to a local optimum (Echeverría et al. 2007, Echeverría & Hemker 2008, Siegler et al. 2016).

The steps of the optimization algorithm used for the trust-region based local optimization problem with utilization of the MM model are the following (Du et al. 2019):

- 1. Setup the initial trust-region radius, λ .
- 2. Evaluate $\mathbf{c}(\mathbf{x})$ and $\mathbf{f}(\mathbf{x})$ at the current design location, $\mathbf{x}^{(i)}$.

- 3. Construct the MM multifidelity model, $\mathbf{s}(\mathbf{x})$.
- 4. Search for the optimal design $\mathbf{x}^{(i+1)}$ in the trust-region using the MM model and a gradient-free optimizer.
- 5. Evaluate $\mathbf{c}(\mathbf{x})$ and $\mathbf{f}(\mathbf{x})$ at $\mathbf{x}^{(i+1)}$ and calculate the gain ratio $\gamma = \frac{(\mathbf{s}(\mathbf{x}^{(i+1)}) \mathbf{f}(\mathbf{x}^{(i)}))}{(\mathbf{f}(\mathbf{x}^{(i+1)}) \mathbf{f}(\mathbf{x}^{(i)}))}$
- 6. Update the trust-region radius, λ , based on the gain ratio, γ , using standard updating rules, i.e., if $\gamma > 0.75$, $\lambda = 2\lambda$ and if $\gamma < 0.25$, $\lambda = \lambda/3$.
- 7. If $\gamma > 0$, update the current design with the optimal design from Step 4.
- 8. Evaluate the stopping criteria. Stop if $||\mathbf{x}^{(i+1)} \mathbf{x}^{(i)}||_2 \le 10^{-4}$ and $||f^{(i+1)} f^{(i)}|| < 10^{-6}$ and $\lambda \le 10^{-4}$, otherwise update the iteration index, i = i + 1, and go to Step 2.

The critical parts of the above optimization framework is the accurate development of the local surrogate $\mathbf{s}^{(i)}(\mathbf{x})$ that is consistent with the HF model locally and the selection of the trust-region radius at each iteration. The accuracy of the MM surrogate model particularly depends on the assumption that similarity between the HF and LF model holds (Echeverría & Hemker 2008). This assumption means that the LF and HF models should exhibit similar local behavior in the region of interest and the surrogate optimization does not introduce a spurious global optimum near the true minimizer \mathbf{x}_f^* (Echeverría & Hemker 2008). In practice, such similarity conditions usually hold, however, it is not necessarily true that every LF model can be successfully used within the MM framework (Echeverría & Hemker 2008).

Additionally, the selection of the initial trust-region radius is important. The number of iterations in the optimization framework could be reduced by searching a large trust-region radius, thereby reducing overall optimization cost. The MM model, however, could be inaccurate which could lead to larger step sizes and, thereby, increasing the number of iterations for the optimization. Therefore, it necessary to select an appropriate LF model and an initial trust-region radius such that the cost of optimization can be kept to a minimum. The focus of this work is to investigate whether the similarity assumption holds when using MM and LF models based on coarse discretization for the multifidelity prediction of airfoil dynamic stall.

Computational fluid dynamics modeling

This section presents the CFD model setup, the HF model validation, and the LF modeling considered in this study. First, the governing equations and the flow solver used in this work are described. Next, the computational grid setup is described, followed by the grid and time-independence study results. The results of the validation of the HF model against experimental data are given. Lastly, the LF model used in this study for the generation of local surrogate models is presented.

3.1 **Governing equations**

In this work, a compressible URANS solver is used for the fluid flow simulation. The time-averaging of Navier-Stokes equations gives the RANS formulation (Wilcox et al. 1998). In particular, for the treatment of compressible flows of gases, mass-weighted averaging is convenient (Anderson et al. 2016). Such averaging is known as the Favre average where $\tilde{f} = \frac{\overline{\rho f}}{\bar{\rho}}$ and f'' are the Favre mean and Favre fluctuating components. The application of the classical Favre averaging to the conservation of mass, momentum, and energy equations gives the URANS equations (Anderson et al. 2016):

$$\frac{\partial \bar{\rho}}{\partial t} + \frac{\partial}{\partial x_i} (\bar{\rho} \, \tilde{u}_i) = 0,\tag{14}$$

$$\frac{\partial}{\partial t}(\bar{\rho}\,\tilde{u}_i) + \frac{\partial}{\partial x_j}(\bar{\rho}\,\tilde{u}_i\,\tilde{u}_j) = \frac{\partial\bar{p}}{\partial x_i} + \frac{\partial\tilde{\tau}_{ij}}{\partial x_j} - \frac{\partial}{\partial x_j}(\overline{\rho\,u_i^"u_j^"}),\tag{15}$$

$$\frac{\partial}{\partial t}(\bar{\rho}\tilde{H}) + \frac{\partial}{\partial x_{i}}(\bar{\rho}\tilde{u}_{j}\tilde{H} + \overline{\rho u"H"} - k\frac{\partial \bar{T}}{\partial x_{j}}) = \frac{\partial \bar{\rho}}{\partial t} + \frac{\partial}{\partial x_{j}}(\tilde{u}_{i}\bar{\tau}_{ij} + \overline{u''_{i}\tau_{ij}}), \tag{16}$$

where ρ , p, u_i , T, H, and τ_{ij} are the density, pressure, velocity component, temperature, total enthalpy, and viscous stress tensor, respectively. The term $-\overline{\rho u_i^{"} u_i^{"}}$ is known as the Reynolds stress, which represents the effects of turbulent fluctuations in the fluid flow and is given as

$$-\overline{\rho u_i^{"} u_j^{"}} = \mu_t \left(\frac{\partial u_i}{\partial x_i} + \frac{\partial u_j}{\partial x_i} - \frac{2}{3} \frac{\partial u_k}{\partial x_k} \delta_{ij} \right) - \frac{2}{3} \rho k \delta_{ij}, \tag{17}$$

where k_t is turbulent kinetic energy, μ_t is the turbulent eddy viscosity, and δ_{ij} is the Kronecker delta function. The Reynolds stress is modeled by one- or two-equation turbulence models to close the URANS equations (14)-(16). In this study, the Navier-Stokes closure problem is solved by applying Menter's shear stress transport (SST) (Menter 1994) as the turbulence model. Menter's SST model has shown an acceptable level of performance in capturing the formation, convection and shedding of DSV for dynamic stall cases (Wang et al. 2010, Hand et al. 2017, Daróczy et al. 2015).

3.2 Flow solver

For this study, Stanford University Unstructured (SU²) is utilized as the numerical solver, which has been extensively validated over a range of compressible turbulent fluid flow problems (Palacios et al. Grapevine (Dallas/Ft. Worth Region,N). SU² provides a dual time stepping strategy (Palacios et al. Grapevine (Dallas/Ft. Worth Region) for unsteady simulations to achieve high-order time accuracy. This method transforms the unsteady problem into a steady problem at each physical time step, which is then solved with well-known convergence acceleration techniques for steady-state problems. Additionally, for dynamic stall simulation, SU² offers grid motion in which convective fluxes are adjusted to take the grid motion into account.

In this study, the dynamic stall simulations are conducted using the URANS solver with the dual time-stepping strategy and rigid grid motion. The governing equations are discretized using a finite volume method with convective flux for the mean flow equations are computed using the Jameson-Schmidt-Turkel (JST) (Palacios et al. Grapevine (Dallas/Ft. Worth Region) scheme. The turbulence working variables for Menter's SST model are convected using a first-order, scalar upwind method. The viscous flux evaluations are assisted by the calculation of spatial gradients with the Green-Gauss method (Palacios et al. Grapevine (Dallas/Ft. Worth Region). Time discretization is achieved by Euler implicit scheme (Palacios et al. Grapevine (Dallas/Ft. Worth Region) with the maximum Courant-Friedrichs-Lewy (CFL) number selected as 4. Furthermore, a two-level multigrid W-cycle method (Palacios et al. Grapevine (Dallas/Ft. Worth Region) is used for convergence acceleration, and the Cauchy convergence criteria (Abbott 2001) is employed on the drag calculation with 100 elements and Cauchy-epsilon criteria of 10^{-6} .

Computational grid 3.3

The C-grid topology is used in this study is shown in Fig. 3a. The grid is generated using the blockMesh utility available through an open-source CFD software — OpenFOAM (Chen et al. 2014). The blockMesh decomposes the domain geometry into a set of one or multiple three-dimensional hexahedral blocks. The C-type external domain is generated with a radius of 55 chord lengths from the leading-edge of an airfoil and a downstream distance of 60 chord lengths. The mesh is highly refined near the airfoil surface with grid points clustered towards the leading- and trailing-edges to capture small vortices and large gradients, as shown in Fig. 3b. Additionally, a dense grid is used in the boundary layer, which is gradually coarsened away from the airfoil surface to the external domain boundary with a growth ratio of around 1.05. The first layer thickness is selected such that $y^+ \le 0.8$

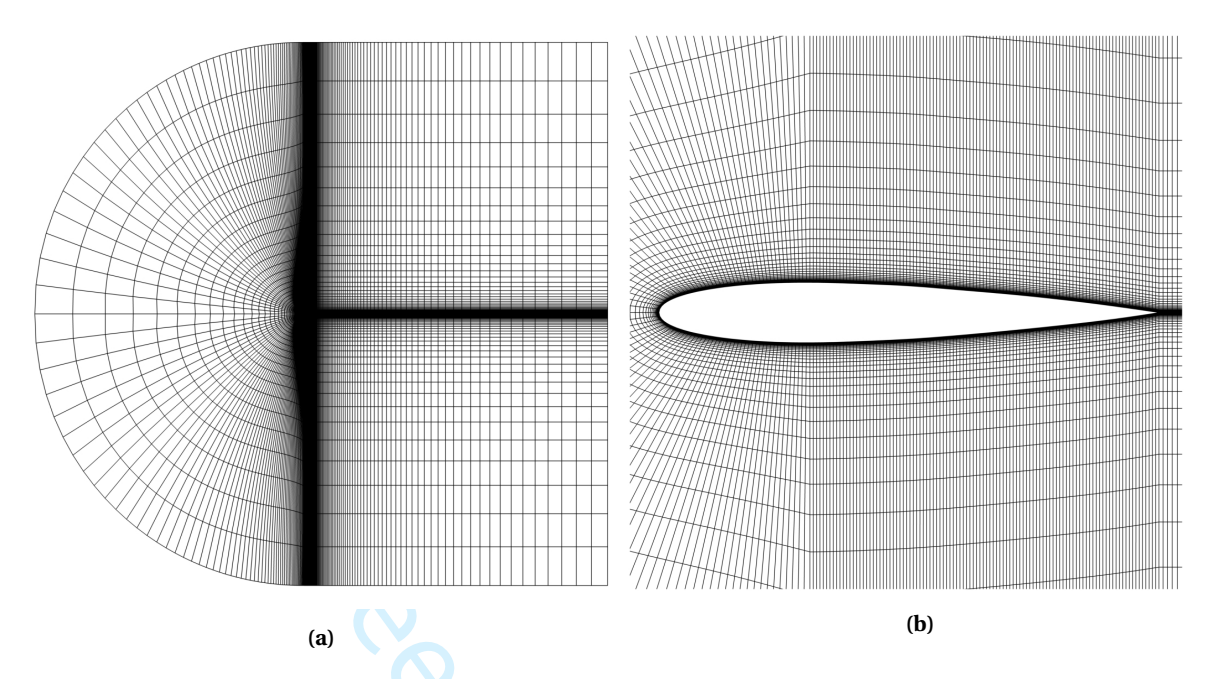


Figure 3: A coarse C-mesh around the NACA 0012 airfoil: (a) the full computational domain, and (b) a view of the mesh close to the airfoil

along the airfoil during the entire pitching cycle. A low y^+ is necessary to capture the onset of dynamic stall vortex accurately. The airfoil surface is modeled as a no-slip adiabatic wall boundary condition, whereas the domain boundary is set as a farfield boundary condition to eliminate boundary reflection. With a similar grid topology, additional grids are generated to perform a grid independence study, as discussed in the next section. Finally, the grid generated using the blockMesh utility is converted to a SU² compatible file format to use with the SU² solver.

Grid and time independence studies

Grid and time independence studies are conducted to establish efficient spatial and temporal resolutions for an accurate unsteady simulation. The spatial resolution is initially determined through a grid sensitivity analysis at a steady-state simulation with a fixed angle. The resulting mesh is then used in the URANS simulation with an oscillating pitching cycle to acquire a physical time step.

The grid independence study is executed at $Re = 135,000,4^{\circ}$ angle of attack, and using the baseline airfoil NACA 0012 with a steady-state RANS solver. A total of 5 grids are generated by subsequently increasing the number of cells in stream-wise, normal and downstream direction by a factor of around 1.2, resulting in meshes in ascending spatial resolution with the finest grid of 720,000 cells and the coarsest grid of 159,000 cells.

The results of the grid independence study are shown in Fig. 4. The grids with the three highest spatial resolutions (cells sizes 387×10^3 , 520×10^3 and 720×10^3) show minimal variations in their

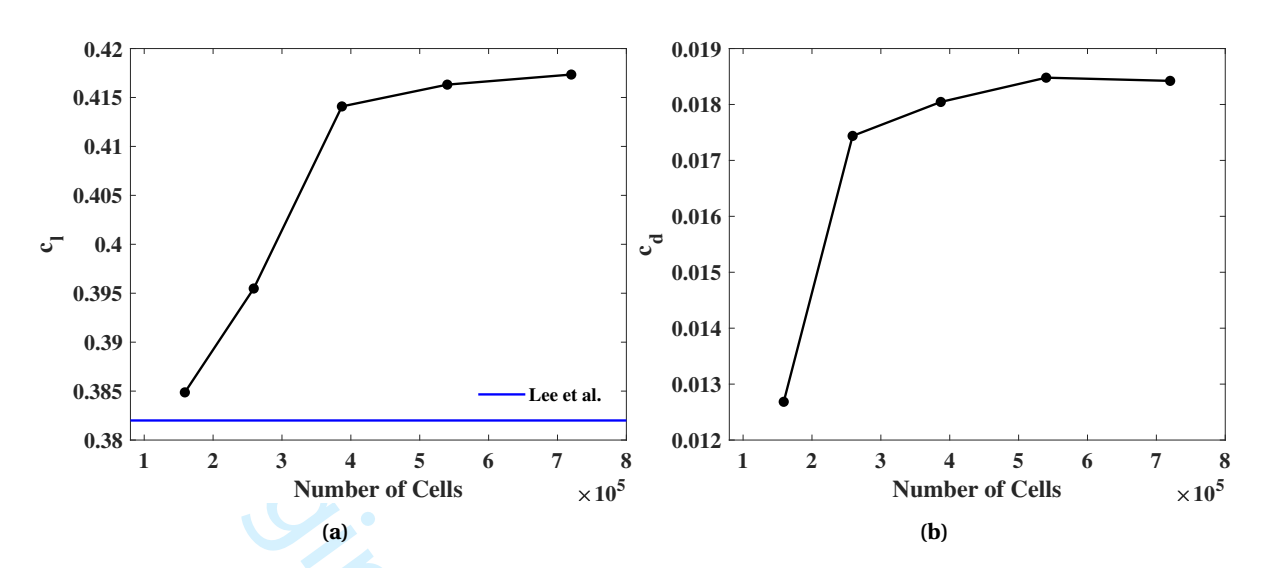


Figure 4: Results of the grid independence study of the NACA 0012 airfoil at Re = 135,000 and an angle of attack of 4° showing the variation in (a) the lift coefficient, and (b) the drag coefficient.

 Table 4: Time step independence study results

d t	$c_{d_{avg}}$	Simulation Time**	$c_{d_{err}} = c_{d_{avg}} - c_{d_{Est}} $
(sec)	(d.c./cycle)	(hrs/cycle)	(d.c.)
0.008	1,813	39	294.5
0.004	2,019	51	88.4
0.002	2,093	65	14.9
0.0015	2,103	69	4.8
0.0010	2,105	78	2.1
0.0005	2,107	99	0.52

^{**}Computed on a high-performance cluster with 112 processors. Wall-clock time.

respective lift coefficients ($\Delta c_l \leq 0.003$) with the drag coefficient variations under 4 d.c. Consequently, the simulation time required for convergence increases with the spatial resolution. The grid with 387×10^3 cells requires almost one third of the time required by the finest grid with 720×10^3 cell. Hence, the grid with 387×10^3 cells is selected for future investigation considering the solution accuracy and computational time requirement.

The selection of physical time-step is made by using the generalized Richardson extrapolation method (REM) (Roy 2003) with the estimation of the average drag coefficient per oscillating cycle ($c_{d_{avg}}$) at a zero time-step, represented as REM estimate, $c_{d_{Est}}$. REM obtains a higher-order estimation of the value under consideration from lower-order values. Table 4 summarizes the REM results. Multiple simulations are conducted with time-steps shown in Table 4 based on which $c_{d_{Est}}$ is estimated as 2,108 d.c. Table 4 also shows the trend of increasing simulation time corresponding to reducing time-step length. Figure 5 shows the trend of $c_{d_{avg}}$ and estimated error $c_{d_{err}}$ against time-step sizes. A time step of 0.0015 sec is selected based on $c_{d_{err}}$ less than 5 d.c metric with a lowest possible simulation time.

Further, to ensure the convergence of the aerodynamic coefficients over the number of cycles, the

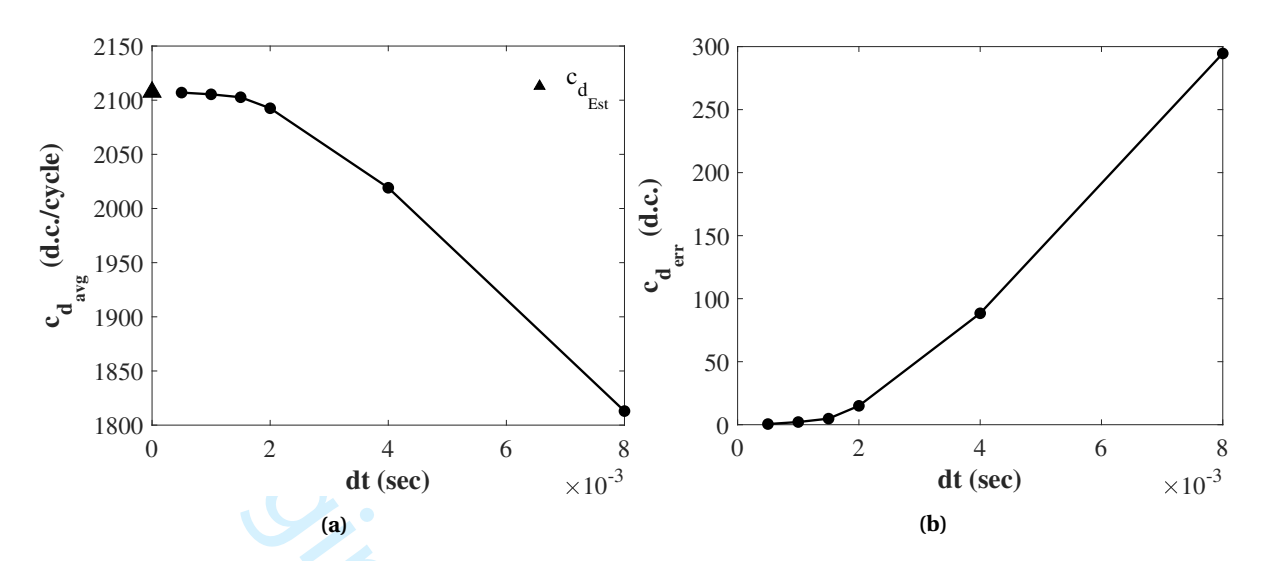


Figure 5: Results of the time step independence study showing (a) the Richardson extrapolation estimate based on the lower order values, and (b) the estimated error from Richardson extrapolation.

mean square error (MSE) between consecutive cycles is computed as

$$MSE = \frac{1}{T_N} \sum_{i=1}^{T_N} (A_j - A_{j+1})_i^2,$$
(18)

where the parameters j and j+1 represent consecutive cycles, T_N represents the total time steps per cycle, and A_j and A_{j+1} represent the aerodynamic coefficients (c_l , c_d or c_m) in consecutive cycles. Simulations are performed over 3.25 cycles using the selected mesh and time step, where the airfoil starts at a mean angle of attack (10°) and undergoes a down-stroke cycle. The data used for the MSE calculations are collected after the lowest angle (-5°) is reached. Table 5 shows the computed MSE between consecutive cycles for aerodynamic coefficients. A minimal error is observed between the first and second cycle aerodynamic coefficients, whereas the second and third cycle produces an almost identical response with negligible MSE. The results ensure that the addition of the initial downstroke part of the cycle is able to stabilize the flow from the abrupt change in rotation rate at the first time step. Thus, it is appropriate to use data after the initial quarter downstroke cycle. In this study, all dynamic stall simulations start with a quarter downstroke cycle, and data is gathered for the remaining part of the pitching cycle.

Table 5: Comparison of mean square error (MSE) between consecutive cycles for lift, drag and pitching moment coefficients with oscillation cycle parameters $\alpha = 10^{\circ} + 15^{\circ} sin(\omega t)$, k = 0.05

	MSE						
Cycles	c_l	c_d	c_m				
		(d.c.)					
1-2	4×10^{-4}	0.55	6×10^{-5}				
2-3	9.8×10^{-6}	0.001	5.5×10^{-7}				

3.5 High-fidelity model validation

The current CFD approach is compared against the experimental and LES results (Kim & Xie 2016) obtained for deep dynamic stall test case described in Section 2.1. The computation is performed using the selected grid and physical time-step as mentioned above with the URANS solver and Menter's SST turbulence model for over 1.25 times the cycle duration. The airfoil initially undergoes a downstroke cycle and data is gathered for the remaining complete cycle. The simulation is run on a high performance computing cluster with 112 processors needing around 69 hours (wall-clock time).

Figure 6 shows the aerodynamic forces and moment response of the NACA 0012 airfoil over the entire pitching cycle. It should be noted that the experimentally obtained aerodynamic forces and moments are the ensemble-average over 100 cycles and computed using pressure signals from pressure taps distributed over the airfoil surface. The LES model result by Kim et al. (Kim & Xie 2016) are ensemble-averaged over 3 cycles. The current CFD results, however, are the time dependent aerodynamic response of over one cycle.

The URANS model shows a reasonable agreement with the LES model results, whereas a qualitative agreement was observed with the experimental results. The essential details of aerodynamic responses of different models are described in Table 6. In terms of the lift coefficient, the URANS model results consistently match with LES model and experiments in the linear region during the upstroke cycle ($\alpha \le$ 16.6°). A similar trend is observed in the pitching moments until $\alpha \leq 16.6^{\circ}$. The URANS prematurely captures the moment stall at 16.6° compared to LES and experiments (Table 6). This is due to the limitation of Menter's SST turbulence model inaccurately identifying the onset of dynamic stall vortex (DSV).

The experimental results in Fig. 6c show a gradual moment stall. In contrast, both computational models observe drastic moment stall, which is affiliated to a sudden change in lift coefficient due to DSV's growth and translation. An abrupt increase in the drag coefficient can also recognize the growth of DSV. The growth and detachment of DSV from the airfoil surface causes dynamic stall resulting in peak lift, drag, and pitching moments (Fig. 6a). The URANS model underpredicts the dynamic stall angle at 19.2° while overpredicting the peak lift, drag, and pitching moment coefficients. After the stall,

Table 6: Comparison of dynamic stall and moment stall location for URANS, LES and experimental data

Models	Moment stall	Dynamic stall
URANS [this work]	16.6°	19.2°
LES (Kim & Xie 2016)	17.8°	19.7°
Experiments (Lee & Gerontakos 2004)	17.3°	20.6°

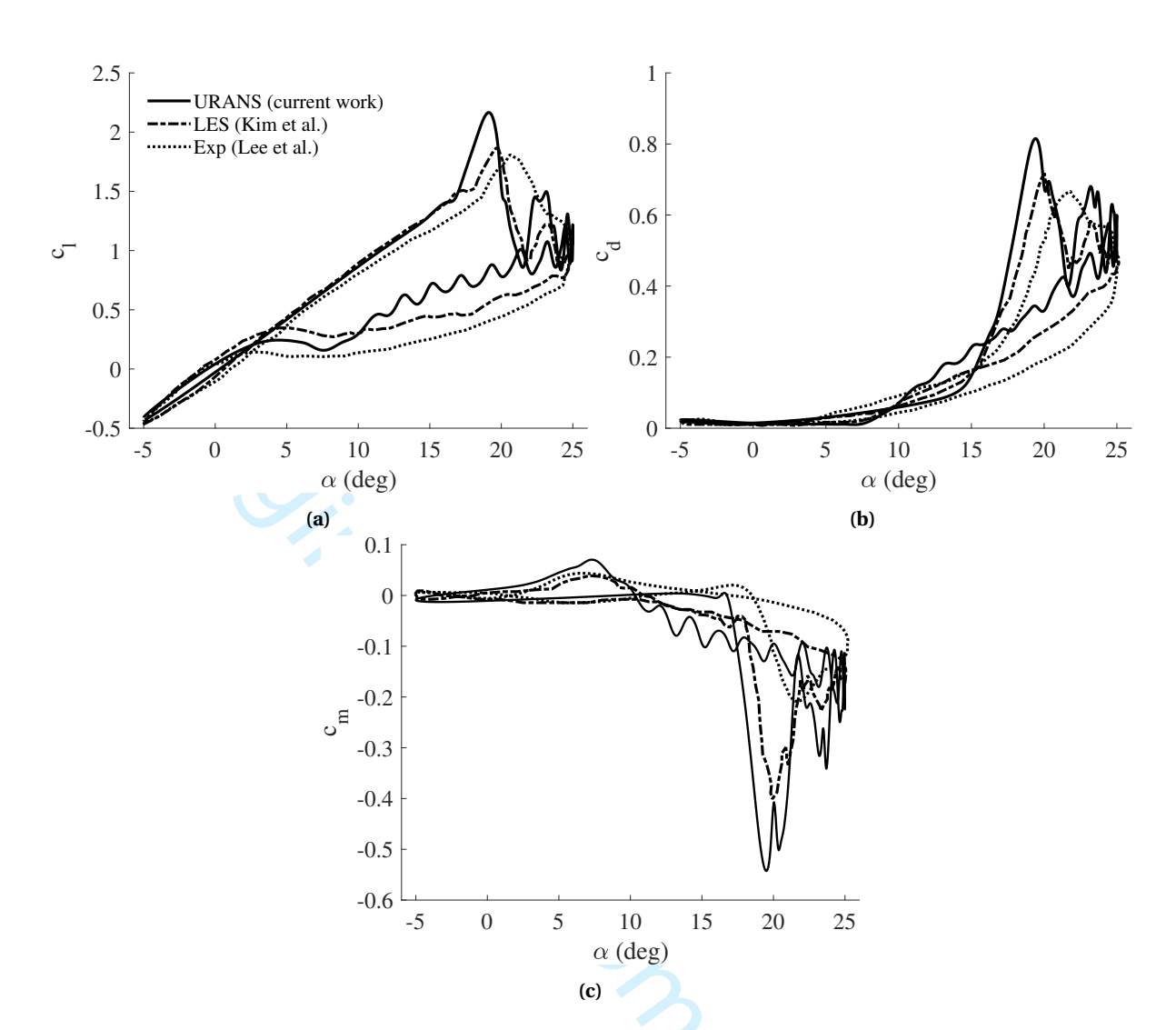


Figure 6: Comparison of time dependent aerodynamic coefficients (a) lift, (b) drag, (c) pitching moment, results for URANS, LES (Kim & Xie 2016) and experiments (Lee & Gerontakos 2004) with oscillation cycle parameters $\alpha = 10^{\circ} + 15^{\circ} sin(\omega t)$, k = 0.05

both the URANS and LES models show the presence of a secondary leading-edge vortex (LEV), while in the experiments such effects are not clear.

Furthermore, the URANS model shows multiple vortex shedding which is observed by the fluctuations in the lift and pitching moment during the downstroke cycle (Figs. 6a and 6c). Such oscillatory behavior was absent from the LES and experimental results. The drag coefficient, in general, shows a less satisfactory agreement with experiments at a higher angle of attack ($\alpha \ge 15^{\circ}$) mostly due to flow separation resulting in an inaccurate modeling of the viscous effects over the airfoil surface (Geng et al. 2018). This compliance worsens, especially in the downstroke cycle, where massive flow separation is present. After the flow reattachment ($\alpha \le 5^{\circ}$), the URANS model starts to show a reasonable agreement with the LES and experimental results.

Although the URANS model can identify the global features of dynamic stall, such as the formation

and convection of the DSV and the dynamic stall progression, the LES model results agree relatively better with the experiments than the URANS model. This is typically due to the deficiencies associated with RANS turbulence models (Mani et al. 2012). The use of LES for ASO of deep dynamic stall cases could produce more accurate results than using RANS models. However, the computational cost for a single LES evaluation is significantly higher, rendering LES currently impractical for optimization studies. The emergence of hybrid RANS-LES models (Rezaeiha et al. 2019, Sanchez-Rocha et al. 2006) could provide a trade-off between LES and RANS by partially resolving the turbulence spectrum (Rezaeiha et al. 2019), thereby alleviating the computational cost compared to LES while providing a viable solution for predicting dynamic stall.

Typically, in optimization studies, multiple CFD evaluations are required within the design space. Thus, using LES and hybrid RANS-LES models in such studies would involve a substantially higher computational cost compared to using only a URANS model. Furthermore, using only the HF URANS model in optimization could become expensive as the number of design evaluations increases quickly with the number of design variables representing the airfoil shape. Therefore, there is a need for a model that could provide a fast but an accurate evaluation within the design space. In this scenario, multifidelity methods can be advantageous, providing an accurate estimation of objective function while saving computational resources and time.

3.6 Low-fidelity modeling

The LF model is the critical ingredient of multifidelity methods as they estimate the output response of the design at a much lower computational cost but generally with lower output accuracy than the HF model (Peherstorfer et al. 2018). The LF model can be generated in various ways (Fernández-Godino et al. 2016): (1) simplifying the mathematical model for representing the physics (e.g., using the Euler inviscid equations as the LF model and the RANS equations for the HF model), (2) changing the discretization of the model (e.g., coarse-grid approximation, early stopping criteria), and (3) using a mathematical model as the LF model and experimental data as the HF model. In fluid-related problems, one of the most popular ways of generating low-fidelity models is by changing the discretization of the HF model (Fernández-Godino et al. 2016).

In this work, the LF models are generated by solving the same governing equations as the HF model but at different combinations of spatial and temporal discretizations. The three mesh sizes and time steps are chosen from Section 3.4, including the mesh size used for generating the HF model. In all the LF models, the convergence criteria are kept the same as the HF model. The HF model and LF model

Table 7: Low-fidelity (LF) and high-fidelity (HF) model configuration used in current study

	Mesh size									
	387k	387k 259k 157k								
	Model	Model Model Model								
dt (sec)										
0.0015	HF	LF1	LF2							
0.008	LF3	LF4	LF5							
0.015	LF6	LF7	LF8							

combinations used in this study are shown in Table 7.

Figure 7 shows the aerodynamic response of the selected LF models against the HF model used for this study. The results are shown only for the upstroke cycle, where DSV formation primarily affects the aerodynamic response. As observed in Fig. 7, the LF model response shows a moderate variation from the HF model selected in our study. The aerodynamic responses of the LF models for $\alpha \leq 15^{\circ}$ are

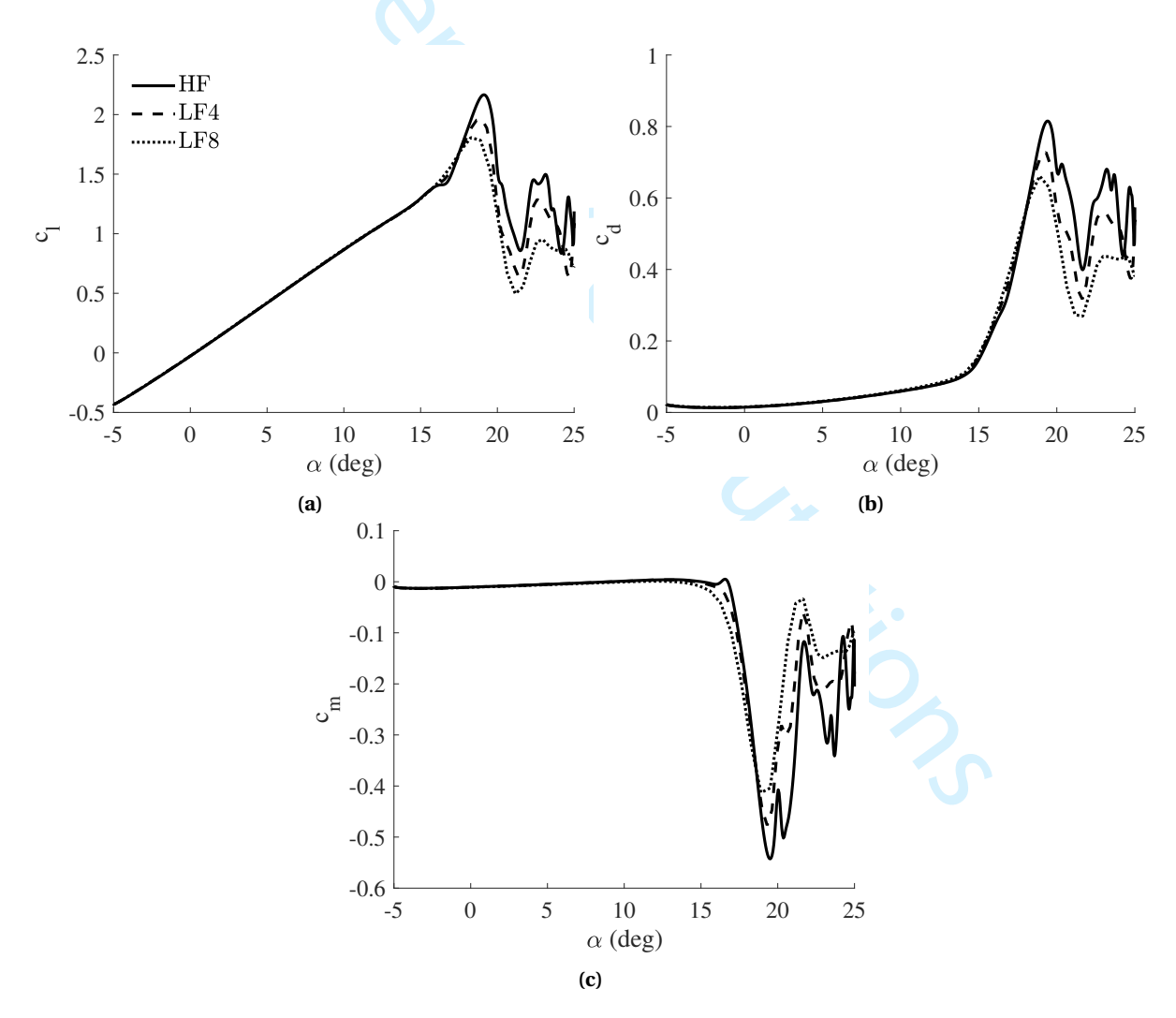


Figure 7: Comparison of time dependent aerodynamic coefficients: (a) lift, (b) drag, (c) pitching moment, results of NACA 0012 airfoil with HF, LF4 and LF8 fidelities with oscillation cycle parameters $\alpha = 10^{\circ} + 15^{\circ} sin(\omega t)$, k = 0.05 (result are shown only for the upstroke cycle)

consistent with the HF model, while the aerodynamic responses for $\alpha \ge 15^{\circ}$ are significantly different due to the lower resolution.

Results

This section presents the results of using the proposed MFM technique for the prediction of dynamic stall. First, the description of the test cases is presented, and then, the individual case results are described.

4.1 Description of test cases

In this study, 100 design samples are generated in the design space $D \subset \mathbb{R}^n$ using Latin hypercube sampling (McKay et al. 2000), where design samples are generated using the uniform distribution between the upper \mathbf{x}_{ub} and lower \mathbf{x}_{lb} bounds of design variable vector (see Table 3). Three pairs of designs are selected from these design samples with increasing distance representing different trustregion radius. The trust-regions are defined based on the Euclidean norm between two normalized design variable vectors, where the design variable vector is normalized with upper bound of design variable vector \mathbf{x}_{uh} . Figure 8 shows the three cases of design pairs selected in current work. Case 1 has the smallest trust-region radius of $\lambda = 0.12$, Case 2 has the trust-region radius of $\lambda = 0.23$, and Case 3 has a trust-region radius of $\lambda = 0.41$. In each case, the initial design ($\mathbf{x}^{(i)}$) is represented by the solid black line whereas the target design ($\mathbf{x}^{(it)}$) is represented by the blue dashed line (Fig. 8).

For this study, eight different LF models are employed with the HF model to construct eight different MM models. All the LF models are obtained by simplifying the HF model with different combinations of spatial and temporal discretizations (see Table 7). The LF models are generated using combinations of three mesh sizes (387k, 259k and 157k) and three time step sizes (0.0015, 0.008 and 0.015 sec).

The performance of MM models is based on the MM model's prediction accuracy of objective function value at target design and the simulation time required for the LF model evaluation. The prediction accuracy of MM model is judged with computation of percentage error given as

error =
$$\frac{s(\mathbf{x}^{(t)}) - f(\mathbf{x}^{(t)})}{f(\mathbf{x}^{(t)})} \times 100,$$
 (19)

where $s(\mathbf{x}^{(t)})$ represents predicted objective function value by MM model at target design $\mathbf{x}^{(t)}$ and $f(\mathbf{x}^{(t)})$ represents objective function value at target design from HF model.

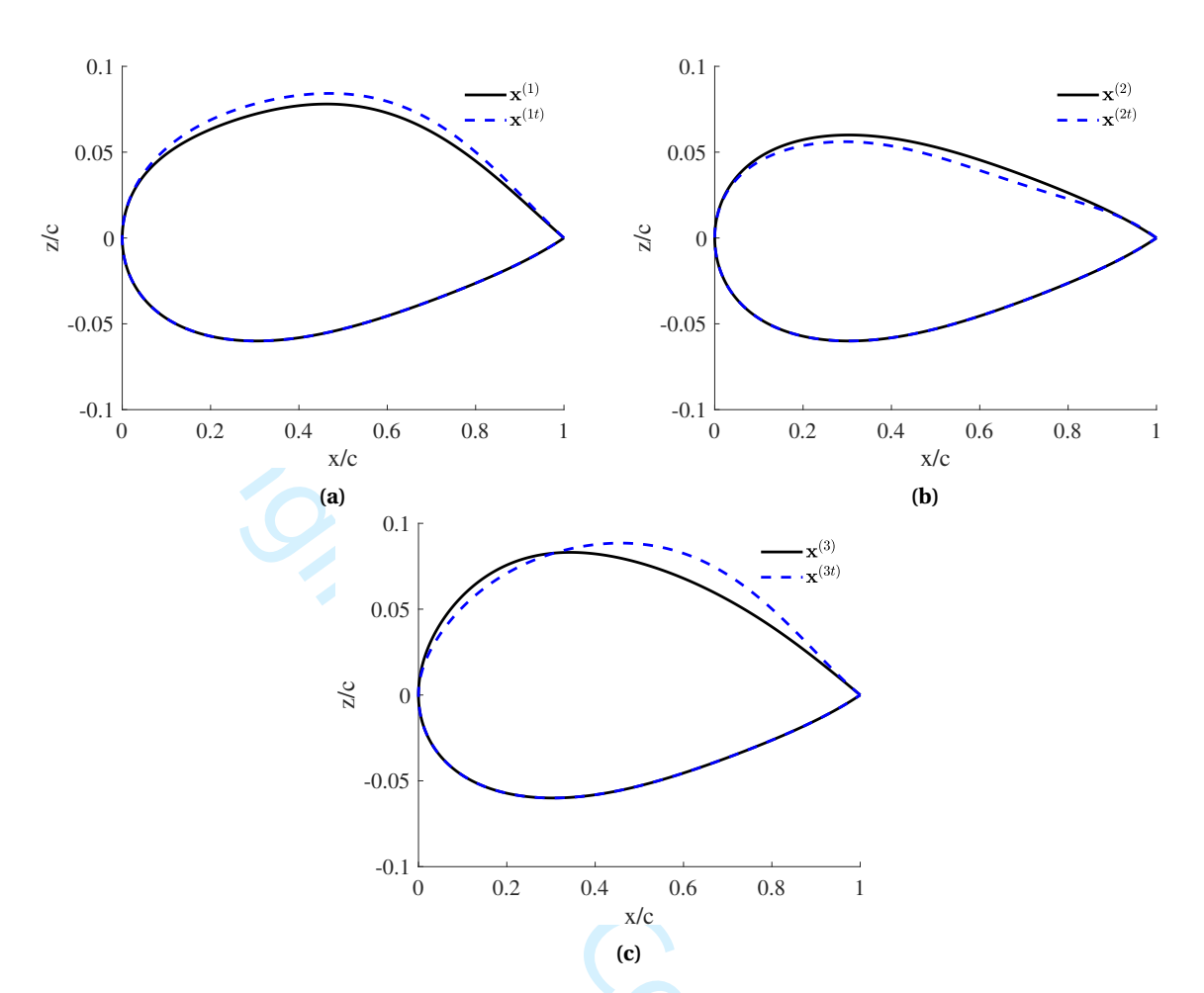


Figure 8: Comparison of airfoil shapes considered in this study (a) Case 1, (b) Case 2, (c) Case 3

4.2 Case 1

Case 1 represents the trust-region radius (λ) of 0.12. In this case, initial design $\mathbf{x}^{(1)}$ is used to construct eight local MM models using an HF model and eight LF models. The HF objective function response at target design $\mathbf{x}^{(1t)}$ is then predicted using the respective MM models. Table 8 shows the performance of the MM model for Case 1, which shows a marginal prediction errors with a maximum error of 2.0% and minimum error of 0.2% when LF6 and LF8 configurations are used for the construction of the MM model, respectively. There is a possibility that the MM model developed from the HF and coarser LF model (for example, LF8) could produce lower errors. The MM model developed with LF8 configuration shows the best performance with 0.2% prediction error and computational speed-up of around 9. In general, the prediction errors in this trust-region are low (\leq 2%), suggesting that the HF-LF model similarity holds that produces a locally accurate MM model.

Figure 9 shows the aerodynamic coefficients obtained by the HF model for Case 1 shapes. It is observed that the aerodynamic coefficients of the initial $\mathbf{x}^{(1)}$ and target $\mathbf{x}^{(1t)}$ shapes are comparable, and they show a similar trend. The dynamic stall and moment stall angles for these shapes are also

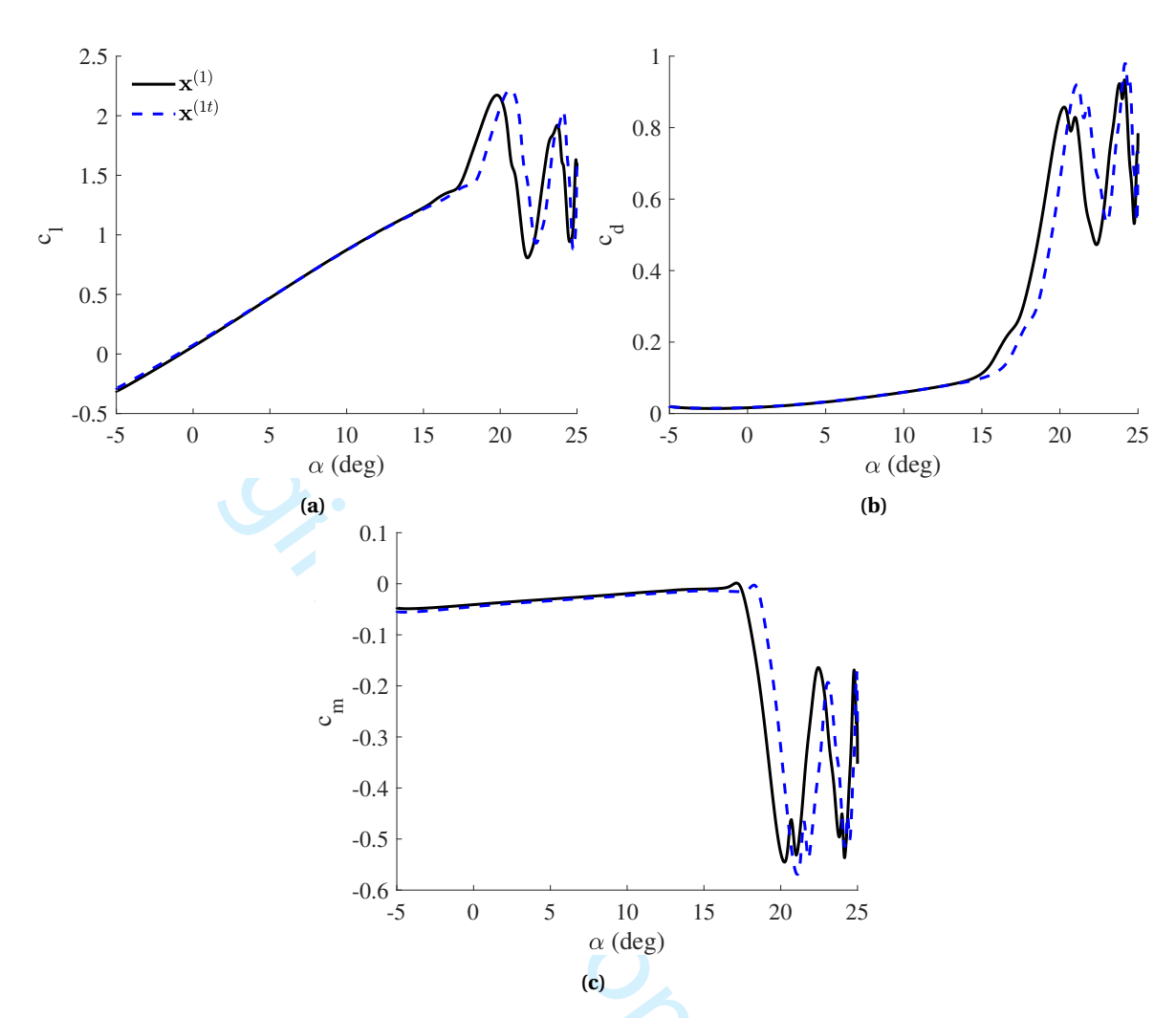


Figure 9: A comparison of HF model response for designs $\mathbf{x}^{(1)}$ and $\mathbf{x}^{(1t)}$ on the basis of (a) lift coefficient, (b) drag coefficient, and (c) pitching moment coefficient.

in close proximity, as seen in Table 9, suggesting a DSV formation at a similar time. The similarity between aerodynamic coefficients of initial $\mathbf{x}^{(1)}$ and target $\mathbf{x}^{(1t)}$ shapes indicates that in lower trust-

Table 8: Performance of MM model with designs $\mathbf{x}^{(1)}$ and $\mathbf{x}^{(1t)}$ (Case 1)

	Mesh size								
	387k			259k			157k		
	Model	error	Time	Model	error	Time	Model	error	Time
		(%)	(hrs)		(%)	(hrs)		(%)	(hrs)
dt (sec)									
0.0015	HF	-	45.7	LF1	0.5	29.1	LF2	1.7	15.9
0.008	LF3	0.6	19.5	LF4	1.0	12.6	LF5	0.2	8.4
0.015	LF6	2.0	11.7	LF7	1.8	7.9	LF8	0.2	5.1

Table 9: Dynamic stall and moment stall angles for Case 1 designs

Airfoil	α_{ds}	α_{ms}
$\mathbf{x}^{(1)}$	19.8°	17.1°
$\mathbf{x}^{(1t)}$	20.6°	18.3°

regions ($\lambda \leq 0.12$), airfoil shapes would produce a similar aerodynamic trend, and the prediction of performance metric by local surrogate would be accurate.

4.3 Case 2

Case 2 design shapes in trust-region radius of $\lambda = 0.23$ are considered. In this case design $\mathbf{x}^{(2)}$ is used as a initial design to construct local MM models and predictions are done at target design $\mathbf{x}^{(2t)}$. Table 10 shows the performance of the MM models for Case 2 designs. The maximum error of 6.9% is observed when LF2 configuration is used for MM model where as minimum error of 0.1% is observed with LF1. The MM model with LF8 configuration shows the lowest simulation time of 5.1 hours while LF7 and LF5 configuration show similar simulation time of around 8 hrs with less than 2% prediction error. In general for Case 2, the LF8 configuration with coarsest mesh and time step shows better performance with prediction error of 1.4% and simulation time of 4.3 hours (computational speed-up of around 9.4. Overall, It is observed that in Case 2 the average prediction errors are slightly higher to 2.5% compared to 1.0% in Case 1.

Figure 10 show the aerodynamic coefficients obtained by evaluating design $\mathbf{x}^{(2)}$ and $\mathbf{x}^{(2t)}$ with HF model. Both shapes show a similar trend in aerodynamic coefficients, as seen in Fig. 10. Furthermore, the dynamic stall and moment stall angles for both designs are similar (see Table 11), indicating that the designs in trust-region $\lambda \le 0.23$ would produce similar dynamic stall characteristics. Thus, considering the aerodynamic trends and the prediction performance of MM models, the trust-region with $\lambda \le 0.23$ could be used for the generation of an accurate local surrogate model.

Table 10: Performance of MM model with designs $\mathbf{x}^{(2)}$ and $\mathbf{x}^{(2t)}$ (Case 2)

		Mesh size							
	387k			259k			157k		
	Model	error	Time	Model	error	Time	Model	error	Time
		(%)	(hrs)		(%)	(hrs)		(%)	(hrs)
dt (sec)									
0.0015	HF	-	40.6	LF1	0.1	25.9	LF2	6.9	14.6
0.008	LF3	2.9	28.6	LF4	1.0	10.7	LF5	3.9	6.9
0.015	LF6	0.2	10.6	LF7	3.7	7.0	LF8	1.4	4.3

Table 11: Dynamic stall and moment stall angles for Case 2 designs

Airfoil	α_{ds}	α_{ms}
$\mathbf{x}^{(2)}$	19.2°	16.6°
$\mathbf{x}^{(2t)}$	18.8°	16.1°

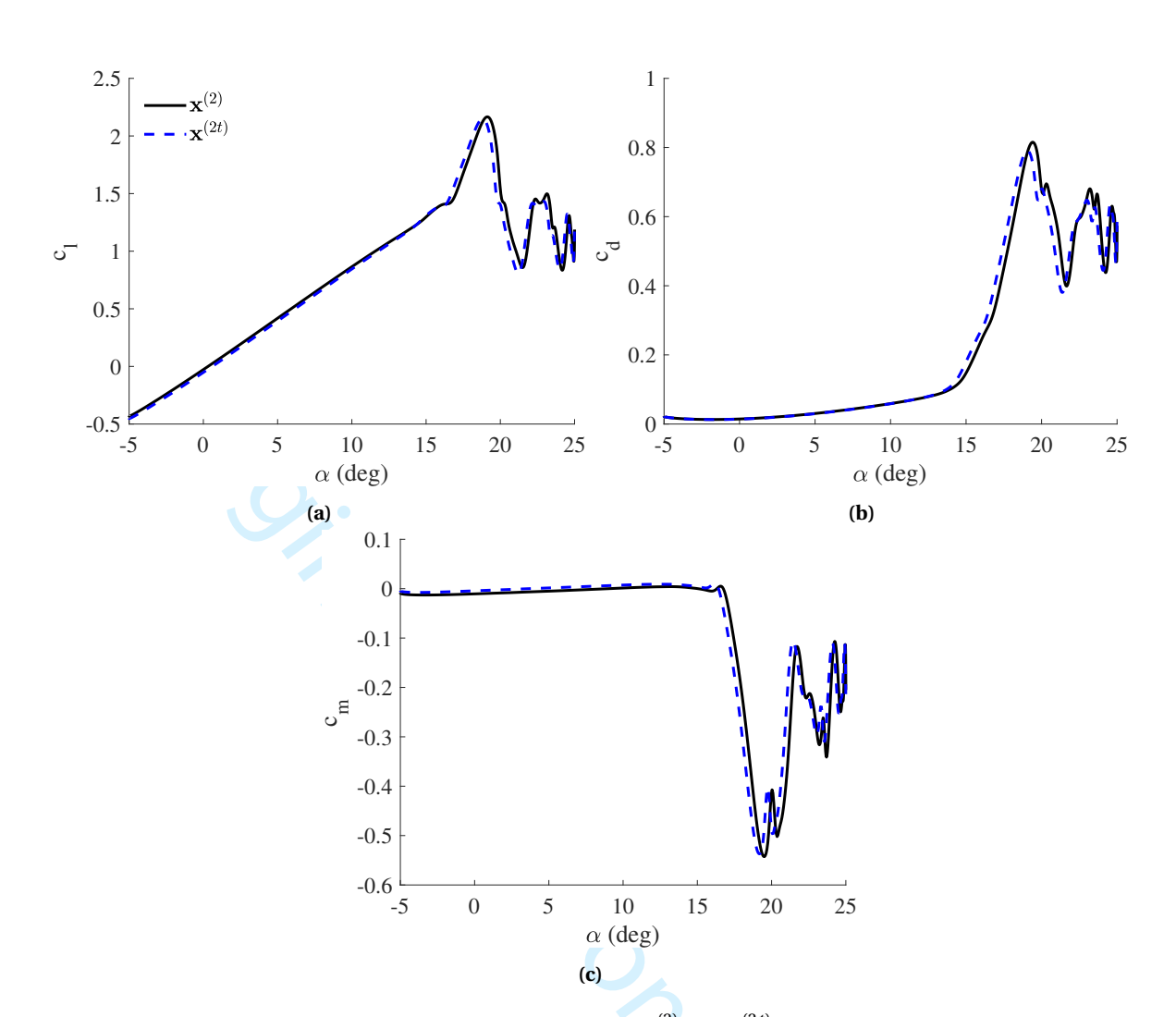


Figure 10: A comparison of HF model response for designs $\mathbf{x}^{(2)}$ and $\mathbf{x}^{(2t)}$ on the basis of (a) lift coefficient, (b) drag coefficient, and (c) pitching moment coefficient.

4.4 Case 3

Case 3 represent the trust-region radius of $\lambda=0.41$ presented by designs $\mathbf{x}^{(3)}$ and $\mathbf{x}^{(3t)}$ as shown in Fig. 8c. Table 12 shows the performance of the MM model for Case 3 with initial design $\mathbf{x}^{(3)}$ used for construction of MM models and prediction of performance metric done at target design $\mathbf{x}^{(3t)}$. It is observed that the average prediction error of (15.2%) in Case 3 is substantially higher than Case 1 and Case 2. The MM model with LF7 configuration shows a maximum prediction error of 25.7%, whereas the MM model with the LF1 configuration shows a minimum error of 1.5%. The higher errors are observed in all three mesh sizes with coarsest time step configuration (LF6, LF7, LF8), while the finer time step configuration shows lower prediction error (LF1, LF2). This could be due to a better similarity between HF and LF models at a fine time discretization as compared to coarser time discretization. Although, the MM models with the LF1 and LF2 configurations show a minimum error less than 3%, they do not provide any significant computational cost-saving for ASO investigations. Additionally, it is

observed that in the larger trust-region radius, the spatial discretization has a lower effect on prediction accuracy than the time discretization suggesting that the HF-LF model similarity deteriorates with coarser time discretization.

Figure 11 shows the time-varying aerodynamic coefficients for designs $\mathbf{x}^{(3)}$ and $\mathbf{x}^{(3t)}$ obtained by HF model evaluation. It is observed that both designs show a very different trend in aerodynamic coefficients, mainly generating from different shapes. This dissimilarity in shape largely affects the dynamic stall characteristics of the design. Table 13 shows dynamic stall and moment stall angle for designs $\mathbf{x}^{(3)}$ and $\mathbf{x}^{(3t)}$. The higher difference between the moment stall angles represents DSV formation at different time, producing much different trends in moment and drag coefficients between the considered designs. Thus, considering the aerodynamic trends and the MM models' prediction accuracy, the trust-region radius $\lambda \ge 0.41$ should be considered only with LF models using finer time discretization.

Overall, in all the three cases (Case 1 to 3), by coarsening the mesh and time step (dt) size, greater computational cost savings are observed. The prediction accuracy of the MM model largely depends on the trust-region radius as seen from Tables 8, 10 and 12. In low to moderate sized trust-regions $\lambda = 0.12$ and 0.23 all the generated MM models showed lower prediction error less than 5%. In general, it is observed that in the smaller trust-region radius, the HF-LF model holds the similarity condition very well, producing higher prediction accuracy. Thus, in smaller trust-regions, LF models generated from coarser spatial and time discretization could be used for constructing MM models producing higher computational savings. In the larger trust-region radius ($\lambda = 0.41$), lower prediction accuracy is observed for the MM models generated from the coarser time discretized LF models. The MM model with fine time discretization showed high prediction accuracy indicating that the HF-LF model similarity holds for LF models that are generated from finer time discretization and the effect of spatial discretization are minimal.

Based on the results obtained from the three cases, Table 14 provides a broad-level recommen-

Table 12: Performance of MM model with designs $\mathbf{x}^{(3)}$ and $\mathbf{x}^{(3t)}$ (Case 3)

	Mesh size								
	387k			259k			157k		
	Model	error	Time	Model	error	Time	Model	error	Time
		(%)	(hrs)		(%)	(hrs)		(%)	(hrs)
dt (sec)									
0.0015	HF	-	44.9	LF1	1.5	28.6	LF2	2.4	16.1
0.008	LF3	15.2	19.9	LF4	14.8	13.1	LF5	15.0	8.9
0.015	LF6	22.8	11.6	LF7	25.7	8.0	LF8	24.8	5.1

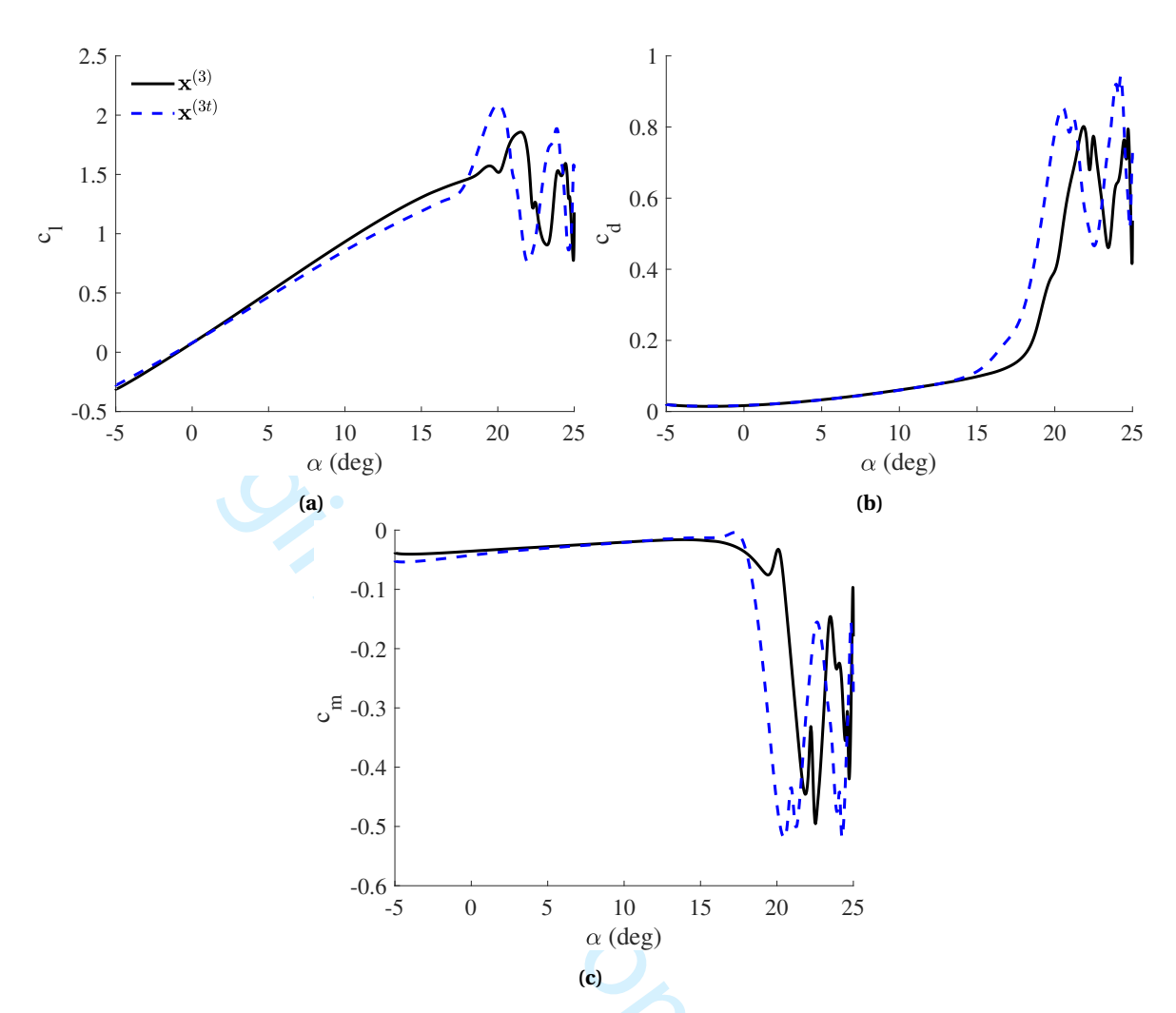


Figure 11: A comparison of HF model response for designs $\mathbf{x}^{(3)}$ and $\mathbf{x}^{(3t)}$ on the basis of (a) lift coefficient, (b) drag coefficient, and (c) pitching moment coefficient.

dation for LF model configuration that could be used to construct an accurate MM model while maintaining HF-LF model similarity for the current problem formulation. In the small to moderate sized trust-regions ($\lambda \leq 0.12$ or $0.12 \leq \lambda \leq 0.23$), all LF models can be used for an accurate construction of MM models with a mean prediction error around 1.0% - 2.5%. However, the MM models using LF5, LF7, or LF8 configurations is recommended based on lower LF model simulation time requirement. The highest computational savings are expected from the MM model developed from the LF8 configuration. For higher trust-region radius ($0.23 \leq \lambda \leq 0.41$) a fine time discretization is recommended. For the current study, the LF2 model with a mean prediction error of around 2.0% and simulation time of around 15 hrs is preferred.

Table 13: Dynamic stall and moment stall angles for Case 3 designs

Airfoil	α_{ds}	α_{ms}
$\mathbf{x}^{(3)}$	21.5°	20.0°
$\mathbf{x}^{(3t)}$	20.0°	17.2°

Table 14: Broad-level recommendation for selection of LF model configuration for different trust-region radii

Trust-region radius	LF Model	Recommended	Mean error	Recommended LF model
λ	acceptable	LF models	(%)	simulation time (hrs)
$\lambda \leq 0.12$	LF1-8	LF5, LF6, LF8	1.0	4 - 9
$0.12 \le \lambda \le 0.23$	LF1-8	LF5, LF6, LF8	1.0-2.5	4 - 9
$0.23 \le \lambda \le 0.41$	LF1, LF2	LF2	2.0	15

Conclusion

In this work, the manifold mapping (MM) method is proposed for the prediction step within a surrogatebased optimization framework utilized for aerodynamic shape optimization (ASO) to mitigate airfoil dynamic stall. The success of MM for finding the optimal designs strongly depends on the similarity between the high- (HF) and low-fidelity (LF) simulation models. This work investigates how to construct accurate local multifidelity models to predict the performance of an aerodynamic surface under dynamic stall and satisfy the similarity assumption at the same time. In the current investigation, the MM technique is implemented for generating eight different local multifidelity models (MFM), based on the HF and eight LF simulation models to predict the HF objective function values in multiple trust-region radii.

It is observed that the trust-region radius significantly affects the prediction accuracy of the local MM model. In a small to medium trust-region radii, all the generated MM models showed lower prediction error less than 5% where HF and LF models hold the similarity condition. In a larger trust-region radius, higher prediction error is observed for MM models constructed from coarser time discretized LF models. This indicates that the time discretization has a more significant effect on the HF-LF model similarity than the spatial discretization, and the HF-LF model similarity deteriorates with coarser time discretization. It is suggested that for the ASO-based dynamic stall mitigation approach, the MM model constructed from the coarser spatial and time discretized LF model in a low to medium trust-region radius can be used efficiently with higher prediction accuracy for the dynamic stall case under consideration.

The approaches used in this study are general and can be used to determine the selection of LF model discretization based on the selected trust-region radius, or vice versa, such that the local MM model will satisfy the similarity condition. In future work, the proposed multifidelity approach, along with the findings from the current work, will be applied to ASO-based dynamic stall mitigation.

Acknowledgements

This material is based upon work supported by the National Science Foundation under award no. 1739551.

References

- Abbott, S. (2001), *Understanding analysis*, Springer-verlag, New York.
- Alexandrov, N. M., Dennis, J., Lewis, R. M. & Torczon, V. (1998), 'A trust-region framework for managing the use of approximation models in optimization', *Structural optimization* **15**(1), 16–23.
- Anderson, D., Tannehill, J. C. & Pletcher, R. H. (2016), Computational fluid mechanics and heat transfer, CRC Press, Boca Raton, United States.
- Andro, J.-Y. & Jacquin, L. (2009), 'Frequency effects on the aerodynamic mechanisms of a heaving airfoil in a forward flight configuration', Aerospace Science and Technology 13(1), 71-80.
- Blom, D., Van Zuijlen, A. & Bijl, H. (2015), 'Multi-level acceleration with manifold mapping of strongly coupled partitioned fluid-structure interaction', Computer Methods in Applied Mechanics and Engineering 296, 211-231.
- Buchner, A., Lohry, M., Martinelli, L., Soria, J. & Smits, A. (2015), 'Dynamic stall in vertical axis wind turbines: comparing experiments and computations', Journal of Wind Engineering and Industrial Aerodynamics 146, 163-171.
- Butterfield, C. P. (1988), Aerodynamic pressure and flow-visualization measurement from a rotating wind turbine blade, Technical report, Solar Energy Research Inst., Golden, CO (USA).
- Butterfield, C. P. (1989), Three-dimensional airfoil performance measurements on a rotating wing, Technical report, Solar Energy Research Inst., Golden, CO (USA).
- Butterfield, C., Simms, D., Scott, G. & Hansen, A. (1991), Dynamic stall on wind turbine blades, Technical report, National Renewable Energy Lab., Golden, CO (United States).
- Carr, L. W. (1988), 'Progress in analysis and prediction of dynamic stall', *Journal of Aircraft* 25(1), 6–17.
- Chen, G., Xiong, Q., Morris, P. J., Paterson, E. G., Sergeev, A. & Wang, Y. (2014), 'Openfoam for computational fluid dynamics', Notices of the AMS 61(4), 354–363.

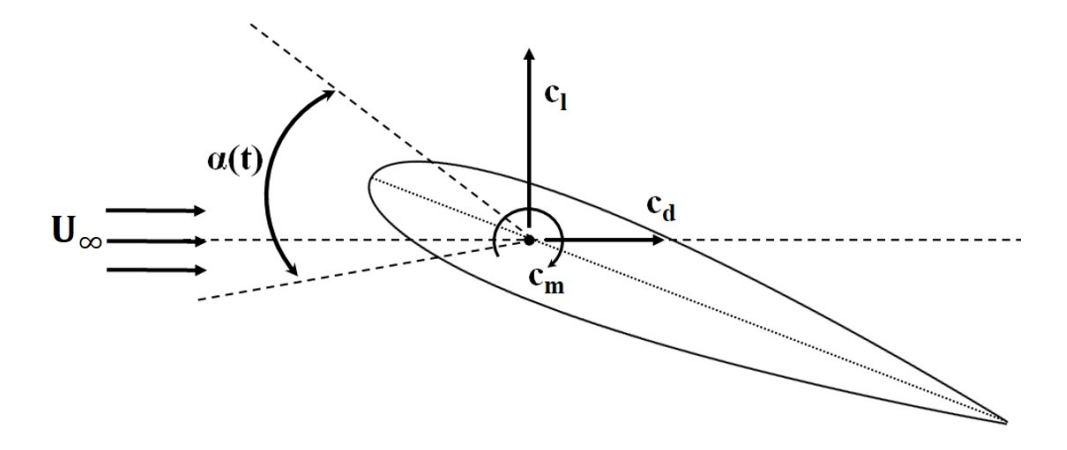
- Daróczy, L., Janiga, G., Petrasch, K., Webner, M. & Thévenin, D. (2015), 'Comparative analysis of turbulence models for the aerodynamic simulation of h-darrieus rotors', Energy 90, 680-690.
- Du, X., Ren, J. & Leifsson, L. (2019), 'Aerodynamic inverse design using multifidelity models and manifold mapping', Aerospace Science and Technology 85, 371–385.
- Echeverría, D. & Hemker, P. (2008), 'Manifold mapping: a two-level optimization technique', Computing and Visualization in Science 11(4-6), 193–206.
- Echeverría, D. et al. (2007), 'Multi-level optimization. space mapping and manifold mapping', *Univer*siteit van Amsterdam, Amsterdam, The Netherlands.
- Economon, T. D., Palacios, F. & Alonso, J. J. (2015), 'Unsteady continuous adjoint approach for aerodynamic design on dynamic meshes', AIAA Journal 53(9), 2437–2453.
- Ellington, C. P. (1999), 'The novel aerodynamics of insect flight: applications to micro-air vehicles', Journal of Experimental Biology 202(23), 3439–3448.
- Ellington, C. P., Van Den Berg, C., Willmott, A. P. & Thomas, A. L. (1996), 'Leading-edge vortices in insect flight', Nature 384(6610), 626.
- Fernández-Godino, M. G., Park, C., Kim, N.-H. & Haftka, R. T. (2016), 'Review of multi-fidelity models', arXiv preprint arXiv:1609.07196.
- Forrester, A., Sobester, A. & Keane, A. (2008), Engineering design via surrogate modelling: a practical guide, John Wiley & Sons, Wiltshire, Great Britain.
- Gardner, A. (2016), Investigations of dynamic stall and dynamic stall control on helicopter airfoils, German Aerospace Center.
- Geng, F., Kalkman, I., Suiker, A. & Blocken, B. (2018), 'Sensitivity analysis of airfoil aerodynamics during pitching motion at a reynolds number of 1.35× 105', Journal of Wind Engineering and Industrial Aerodynamics 183, 315-332.
- Gerontakos, P. & Lee, T. (2006), 'Dynamic stall flow control via a trailing-edge flap', AIAA Journal (3), 469–480.
- Hand, B., Kelly, G. & Cashman, A. (2017), 'Numerical simulation of a vertical axis wind turbine airfoil experiencing dynamic stall at high reynolds numbers', Computers & Fluids 149, 12–30.

- Hemker, P. W. & Echeverría, D. (2007), 'A trust-region strategy for manifold-mapping optimization', *Journal of Computational Physics* **224**(1), 464–475.
- Hu, Y., Zhang, H. & Wang, G. (2018), 'The effects of dynamic-stall and parallel bvi on cycloidal rotor', Aircraft Engineering and Aerospace Technology **90**(1), 87–95.
- Jameson, A. (2003), 'Aerodynamic shape optimization using the adjoint method', *Lectures at the Von Karman Institute*, *Brussels*, *Belgium*.
- Khalfallah, S., Ghenaiet, A., Benini, E. & Bedon, G. (2015), 'Surrogate-based shape optimization of stall margin and efficiency of a centrifugal compressor', *Journal of Propulsion and Power* **31**(6), 1607–1620.
- Kim, Y. & Xie, Z.-T. (2016), 'Modelling the effect of freestream turbulence on dynamic stall of wind turbine blades', *Computers & Fluids* **129**, 53–66.
- Koziel, S., Bandler, J. W. & Madsen, K. (2008), 'Quality assessment of coarse models and surrogates for space mapping optimization', *Optimization and Engineering* **9**(4), 375–391.
- Koziel, S. & Yang, X.-S. (2011), *Computational optimization, methods and algorithms*, Vol. 356, Springer, Berlin Heidelberg, Germany.
- Kumar, D. & Cesnik, C. E. (2015), 'Performance enhancement in dynamic stall condition using active camber deformation', *Journal of the American Helicopter Society* **60**(2), 1–12.
- Laurenceau, J. & Meaux, M. (10th April 2008), Comparison of gradient and response surface based optimization frameworks using adjoint method, *in* '49th AIAA/ASME/ASCE/AHS/ASC Structures, Structural Dynamics, and Materials Conference, 16th AIAA/ASME/AHS Adaptive Structures Conference, 10th AIAA Non-Deterministic Approaches Conference, 9th AIAA Gossamer Spacecraft Forum, 4th AIAA Multidisciplinary Design Optimization Specialists Conference, Schaumburg, IL', p. 1889.
- Lee, T. & Gerontakos, P. (2004), 'Investigation of flow over an oscillating airfoil', *Journal of Fluid Mechanics* **512**, 313–341.
- Lee, T. & Gerontakos, P. (2006), 'Dynamic stall flow control via a trailing-edge flap', *AIAA Journal* **44**(3), 469–480.
- Leifsson, L. & Koziel, S. (2015), *Simulation-driven aerodynamic design using variable-fidelity models*, World Scientific, London, United Kingdom.

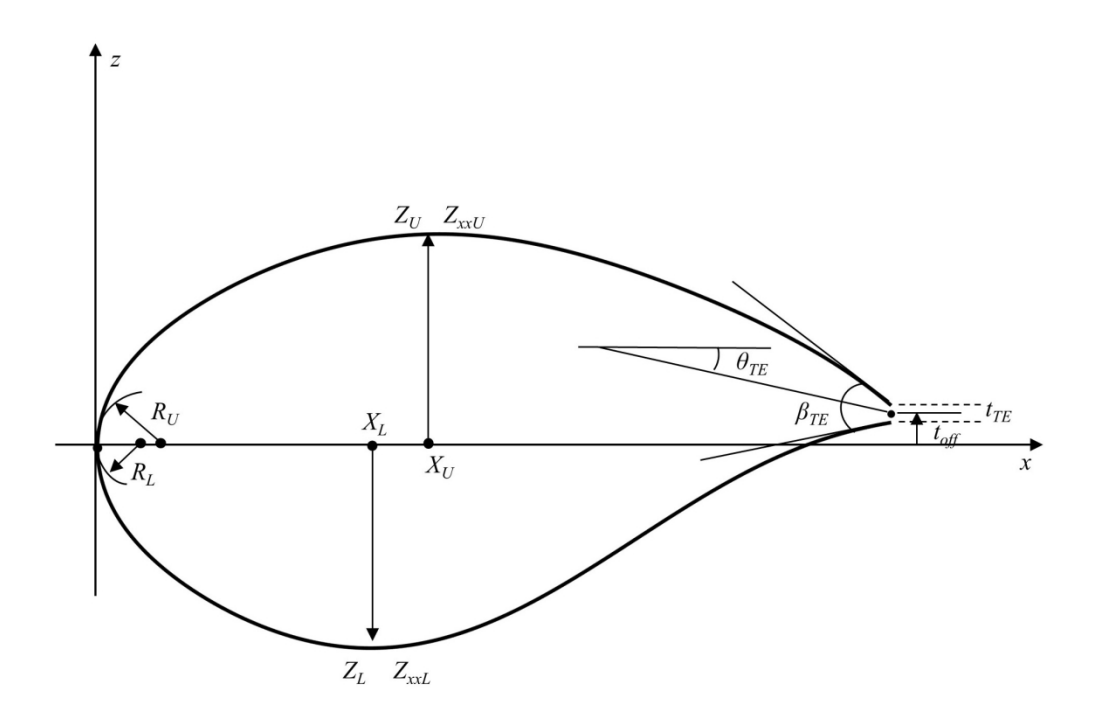
- Mani, K., Lockwood, B. A. & Mavriplis, D. J. (2012), Adjoint-based unsteady airfoil design optimization with application to dynamic stall, in 'American Helicopter Society 68th annual forum proceedings', Vol. 68, American Helicopter Society, Washington, DC.
- McCroskey, W. J., Carr, L. W. & McAlister, K. W. (1976), 'Dynamic stall experiments on oscillating airfoils', Aiaa Journal 14(1), 57-63.
- McKay, M. D., Beckman, R. J. & Conover, W. J. (2000), 'A comparison of three methods for selecting values of input variables in the analysis of output from a computer code', Technometrics 42(1), 55–61.
- Menter, F. R. (1994), 'Two-equation eddy-viscosity turbulence models for engineering applications', AIAA Journal 32(8), 1598-1605.
- Müller-Vahl, H. F., Nayeri, C. N., Paschereit, C. O. & Greenblatt, D. (2016), 'Dynamic stall control via adaptive blowing', Renewable Energy 97, 47-64.
- Nadarajah, S. K. & Jameson, A. (2007), 'Optimum shape design for unsteady flows with time-accurate continuous and discrete adjoint method', AIAA Journal 45(7), 1478–1491.
- Palacios, F., Alonso, J., Duraisamy, K., Colonno, M., Hicken, J., Aranake, A., Campos, A., Copeland, S., Economon, T., Lonkar, A. et al. (Grapevine (Dallas/Ft. Worth Region), Texas, 2013), Stanford university unstructured (su 2): an open-source integrated computational environment for multiphysics simulation and design, in '51st AIAA Aerospace Sciences Meeting including the New Horizons Forum and Aerospace Exposition', p. 287.
- Palacios, F., Economon, T. D., Aranake, A., Copeland, S. R., Lonkar, A. K., Lukaczyk, T. W., Manosalvas, D. E., Naik, K. R., Padron, S., Tracey, B. et al. (National Harbor, Maryland, 13-17 January 2014), Stanford university unstructured (su2): Analysis and design technology for turbulent flows, in '52nd Aerospace Sciences Meeting,', p. 0243.
- Peherstorfer, B., Willcox, K. & Gunzburger, M. (2018), 'Survey of multifidelity methods in uncertainty propagation, inference, and optimization', SIAM Review 60(3), 550–591.
- Raul, V. & Leifsson, L. (2021), 'Surrogate-based aerodynamic shape optimization for delaying airfoil dynamic stall using kriging regression and infill criteria', Aerospace Science and Technology p. 106555.
- Rezaeiha, A., Montazeri, H. & Blocken, B. (2019), 'Cfd analysis of dynamic stall on vertical axis wind turbines using scale-adaptive simulation (sas): Comparison against urans and hybrid rans/les', Energy Conversion and Management 196, 1282–1298.

- Roy, C. J. (2003), 'Grid convergence error analysis for mixed-order numerical schemes', AIAA Journal (4), 595–604.
- Sanchez-Rocha, M., Kirtas, M. & Menon, S. (2006), Zonal hybrid rans-les method for static and oscillating airfoils and wings, in '44th AIAA Aerospace Sciences Meeting and Exhibit', p. 1256.
- Siegler, J., Ren, J., Leifsson, L., Koziel, S. & Bekasiewicz, A. (2016), 'Supersonic airfoil shape optimization by variable-fidelity models and manifold mapping', Procedia Computer Science 80, 1103–1113.
- Simpson, T. W., Poplinski, J., Koch, P. N. & Allen, J. K. (2001), 'Metamodels for computer-based engineering design: survey and recommendations', Engineering with Computers 17(2), 129–150.
- Sobieczky, H. (1999), Parametric airfoils and wings, in 'Recent development of aerodynamic design methodologies', Vieweg+Teubner Verlag, Wiesbaden, Germany, pp. 71–87.
- Tang, J., Hu, Y., Song, B. & Yang, H. (2017), 'Unsteady aerodynamic optimization of airfoil for cycloidal propellers based on surrogate model', Journal of Aircraft 54(4), 1241–1256.
- Thelen, A. S., Leifsson, L. T. & Beran, P. S. (2020), 'Multifidelity flutter prediction using local corrections to the generalized aic', Aerospace Science and Technology 106, 106032.
- Van Den Berg, C. & Ellington, C. P. (1997), 'The vortex wake of a hovering model hawkmoth', Philosophical Transactions of the Royal Society of London B: Biological Sciences 352(1351), 317–328.
- Vu, N. & Lee, J. (2015), 'Aerodynamic design optimization of helicopter rotor blades including airfoil shape for forward flight', Aerospace Science and Technology 42, 106–117.
- Wang, Q. & Zhao, Q. (2018), 'Rotor airfoil profile optimization for alleviating dynamic stall characteristics', Aerospace Science and Technology 72, 502-515.
- Wang, Q., Zhao, Q. & Wu, Q. (2015), 'Aerodynamic shape optimization for alleviating dynamic stall characteristics of helicopter rotor airfoil', Chinese Journal of Aeronautics 28(2), 346-356.
- Wang, S., Ingham, D. B., Ma, L., Pourkashanian, M. & Tao, Z. (2010), 'Numerical investigations on dynamic stall of low reynolds number flow around oscillating airfoils', Computers & Fluids 39(9), 1529-1541.
- Wilcox, D. C. et al. (1998), Turbulence modeling for CFD, Vol. 2, DCW industries La Canada, CA.

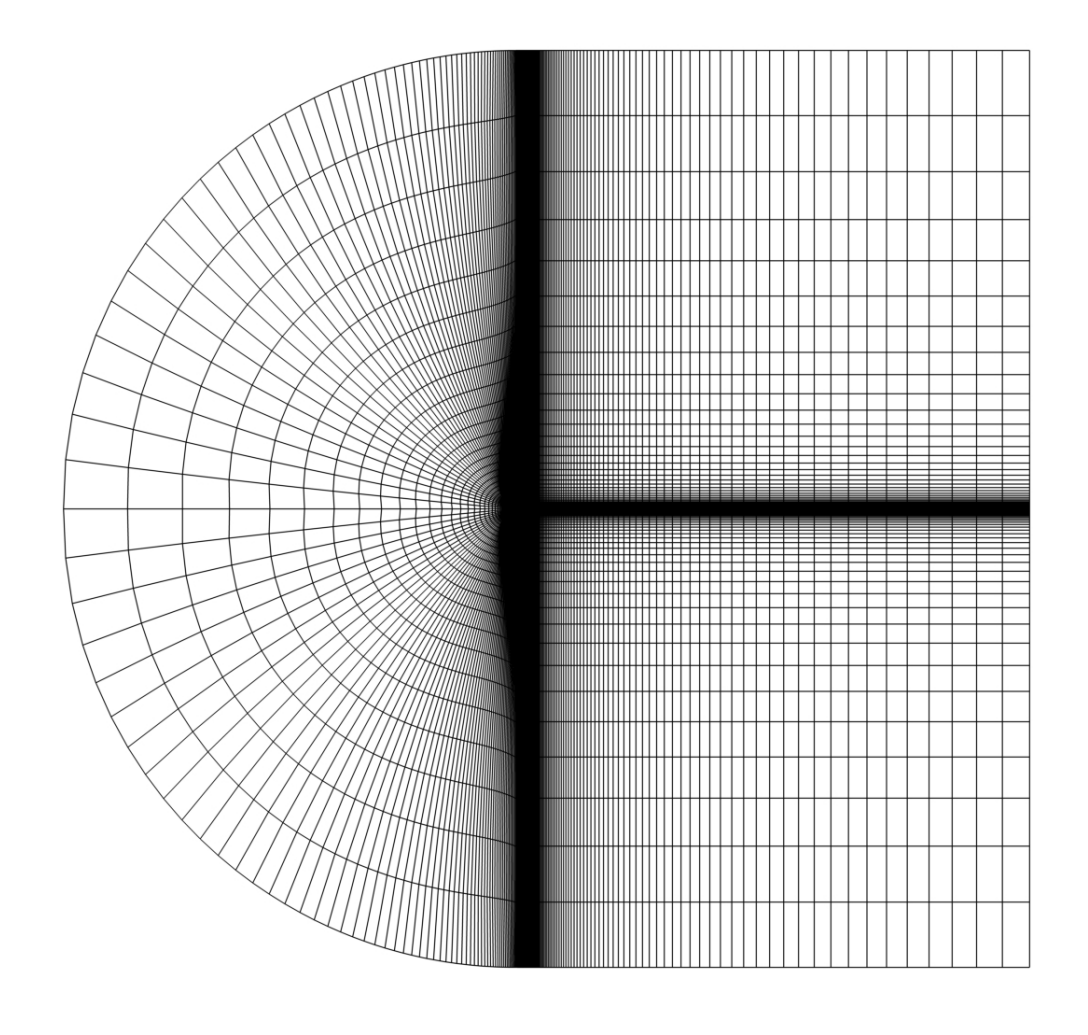
- Wong, T., O Malley, J. & O Brien, D. (2006), Investigation of effect of dynamic stall and its alleviation on helicopter performance and loads, in 'Annual Forum Proceedings-American Helicopter Society', Vol. 62, p. 1749.
- Yu, Y. H., Lee, S., McAlister, K. W., Tung, C. & Wang, C. M. (1995), 'Dynamic stall control for advanced rotorcraft application', AIAA Journal 33(2), 289–295.
- Zhao, G.-q. & Zhao, Q.-j. (2015), 'Dynamic stall control optimization of rotor airfoil via variable droop leading-edge', Aerospace Science and Technology 43, 406–414.
- Zhou, Z., Ong, Y. S., Nguyen, M. H. & Lim, D. (2005), A study on polynomial regression and gaussian process global surrogate model in hierarchical surrogate-assisted evolutionary algorithm, in '2005 IEEE congress on evolutionary computation', Vol. 3, IEEE, Edinburgh, Scotland, UK, pp. 2832–2839.



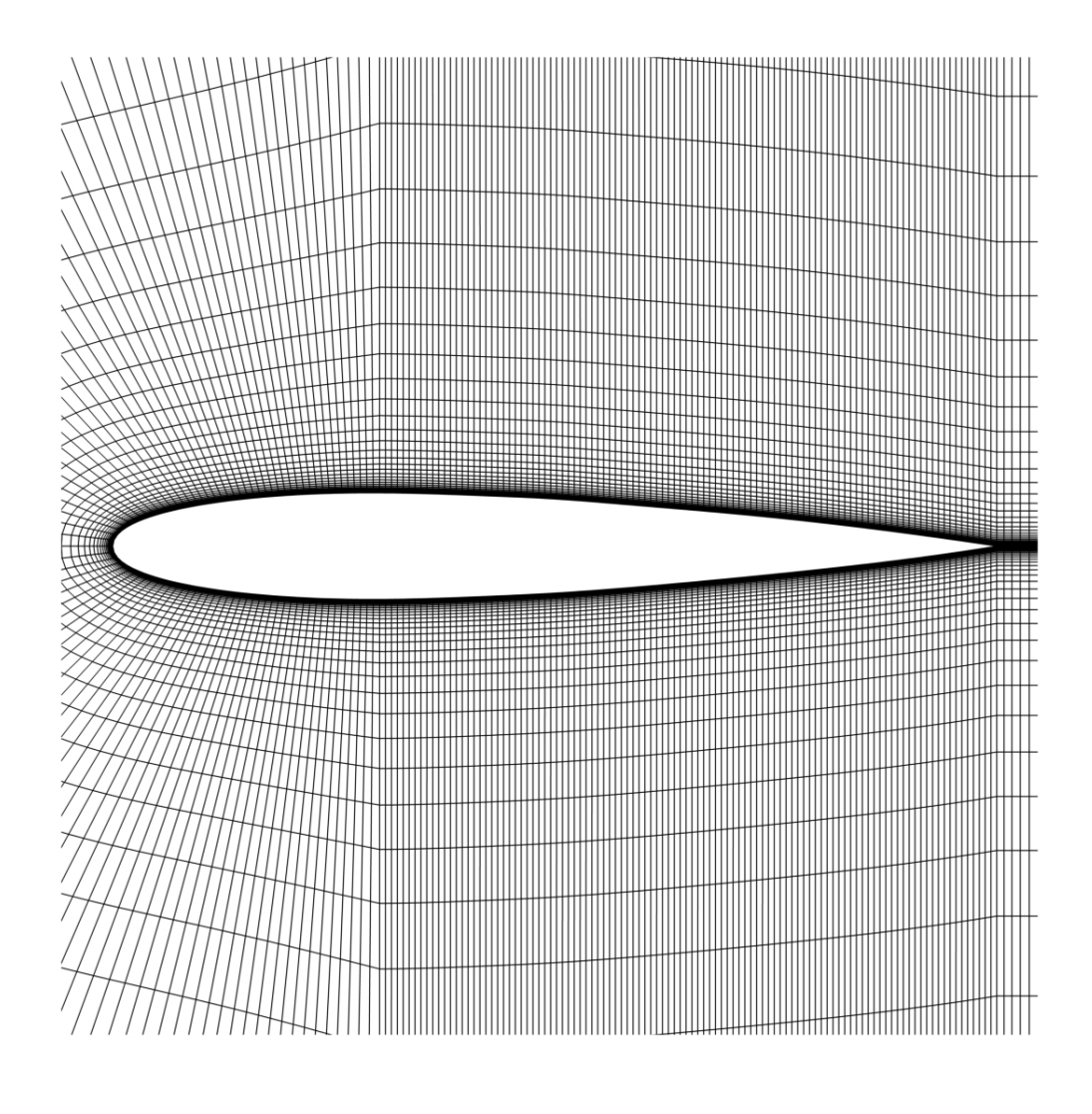
192x79mm (150 x 150 DPI)



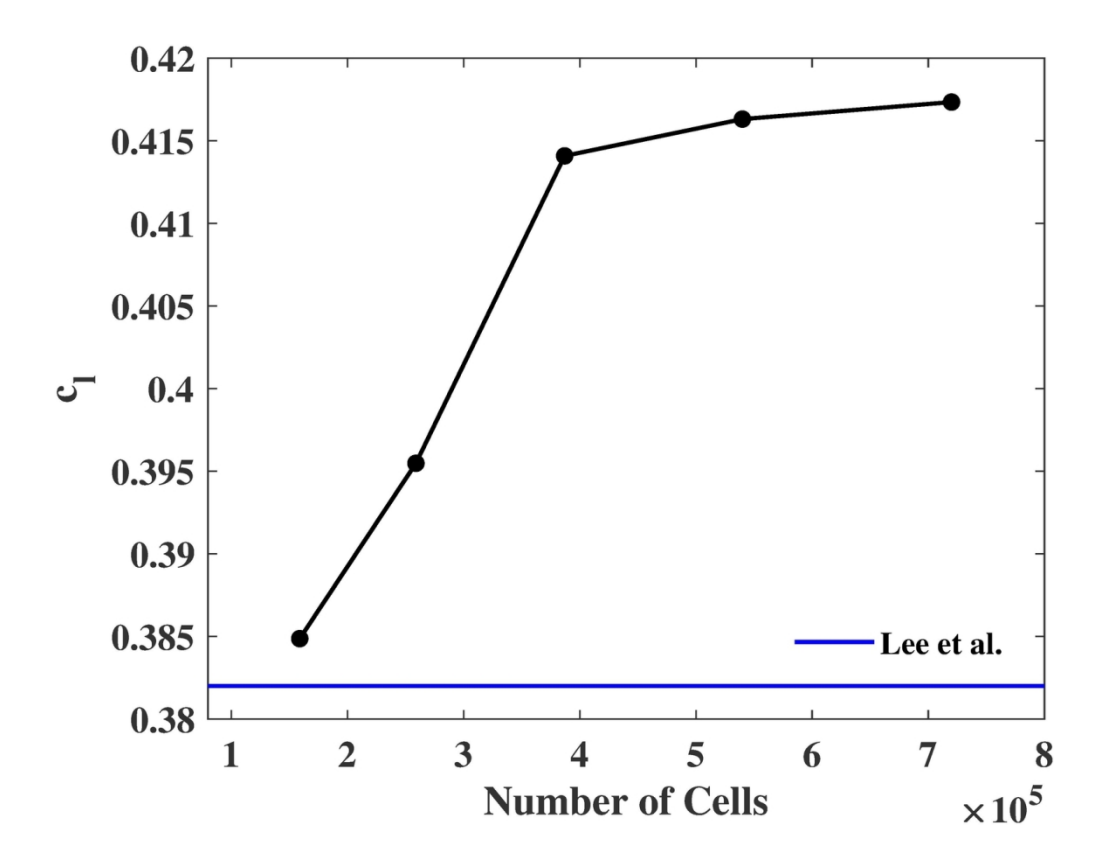
164x108mm (300 x 300 DPI)



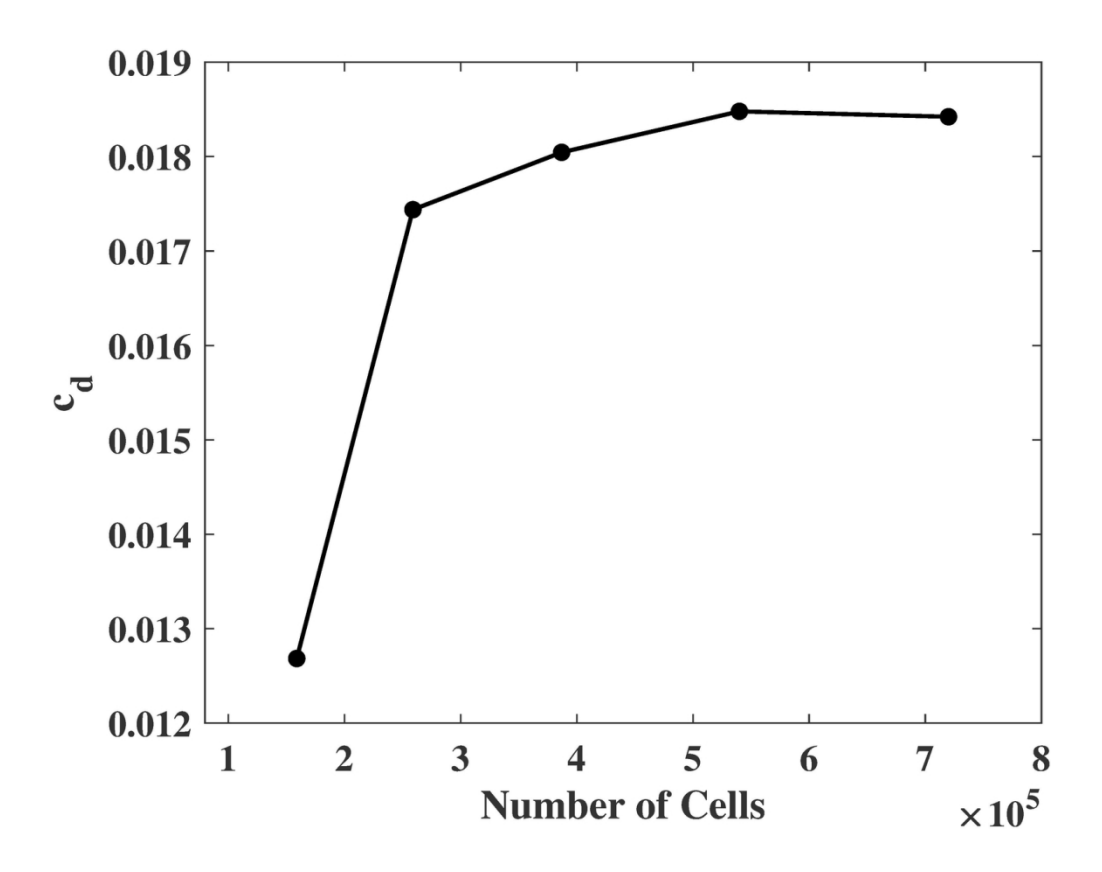
378x378mm (72 x 72 DPI)



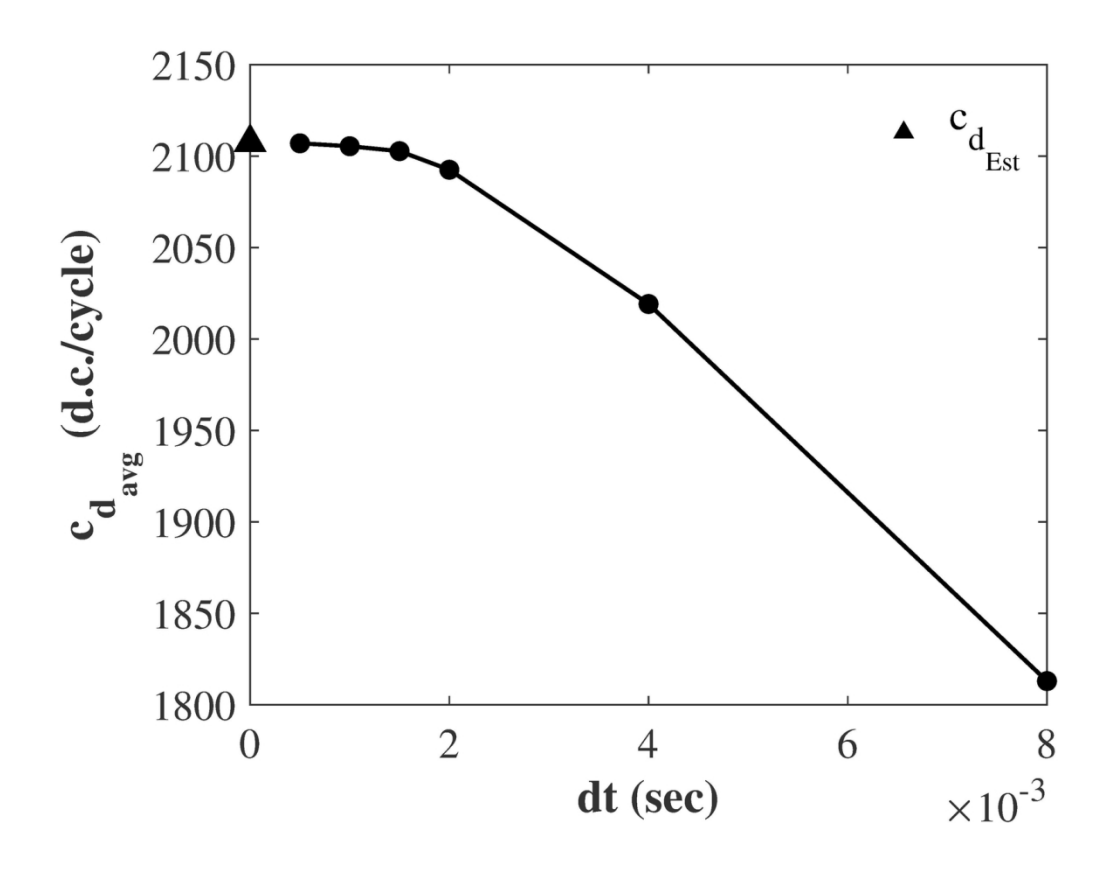
378x378mm (72 x 72 DPI)



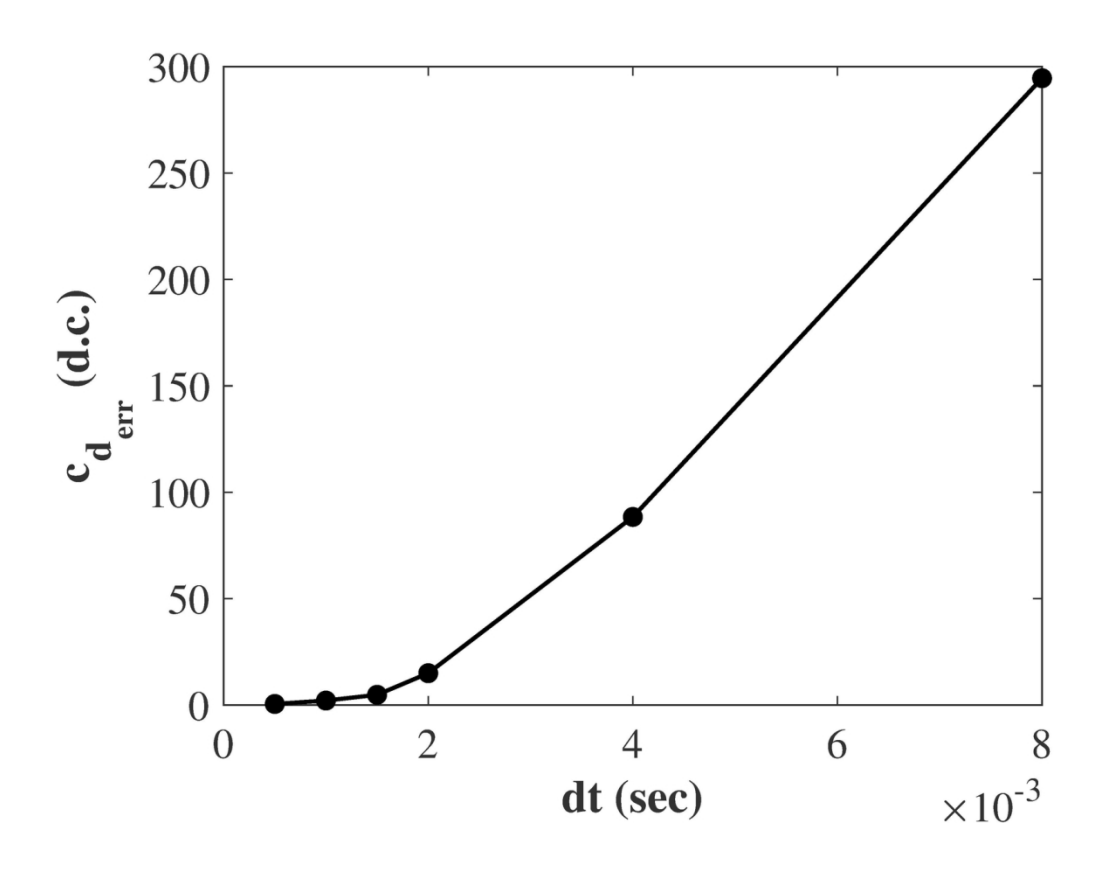
133x104mm (300 x 300 DPI)



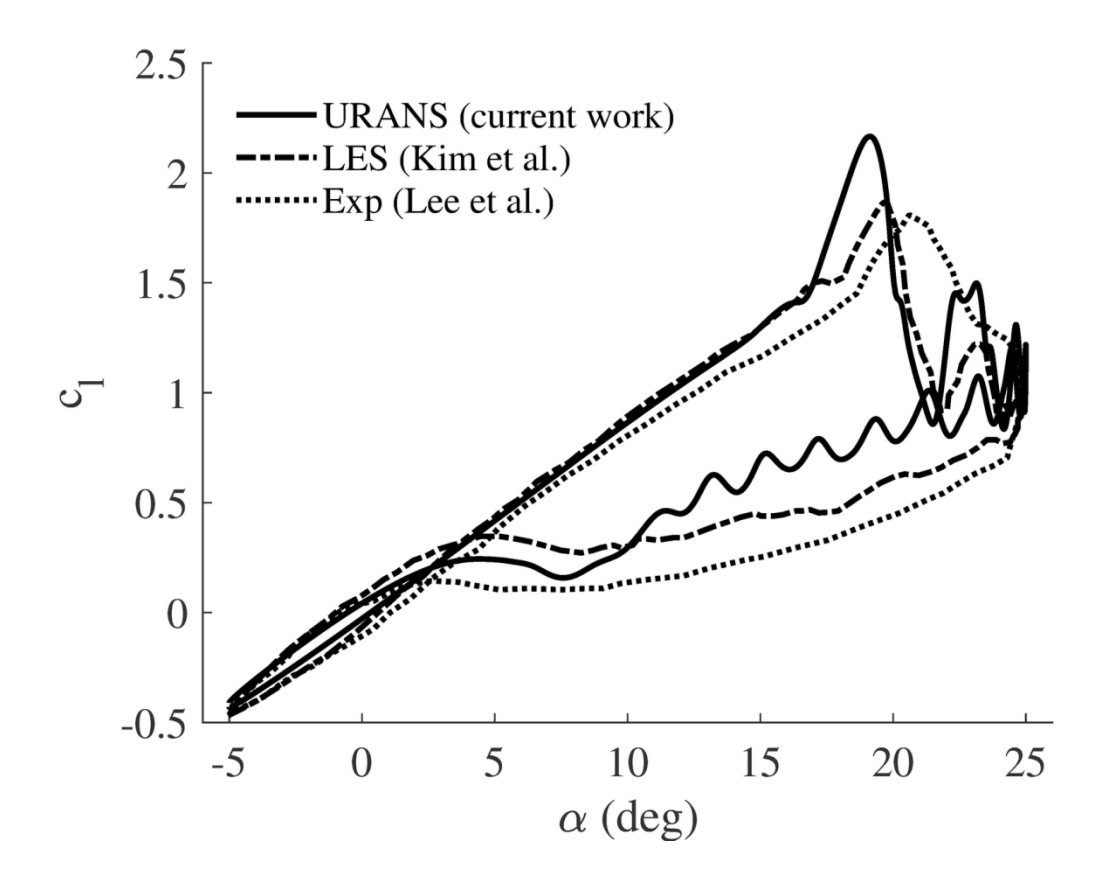
133x104mm (300 x 300 DPI)



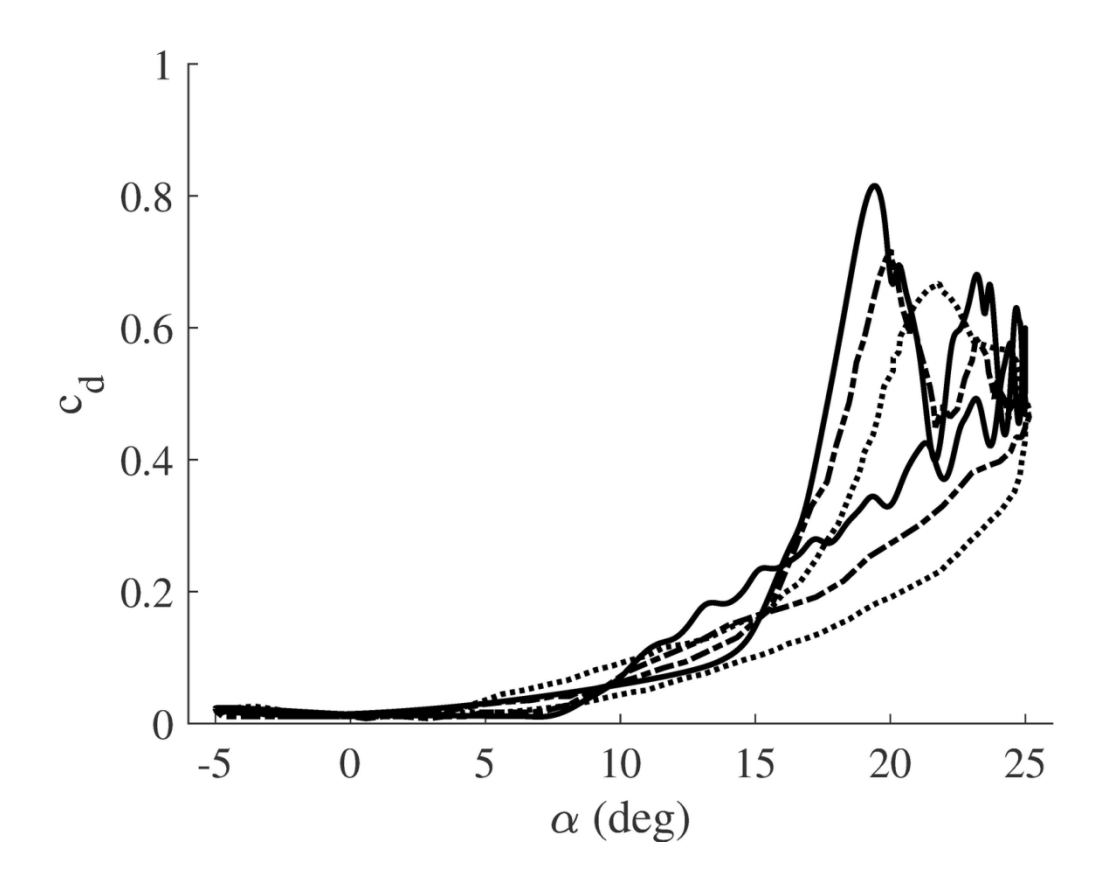
134x104mm (300 x 300 DPI)



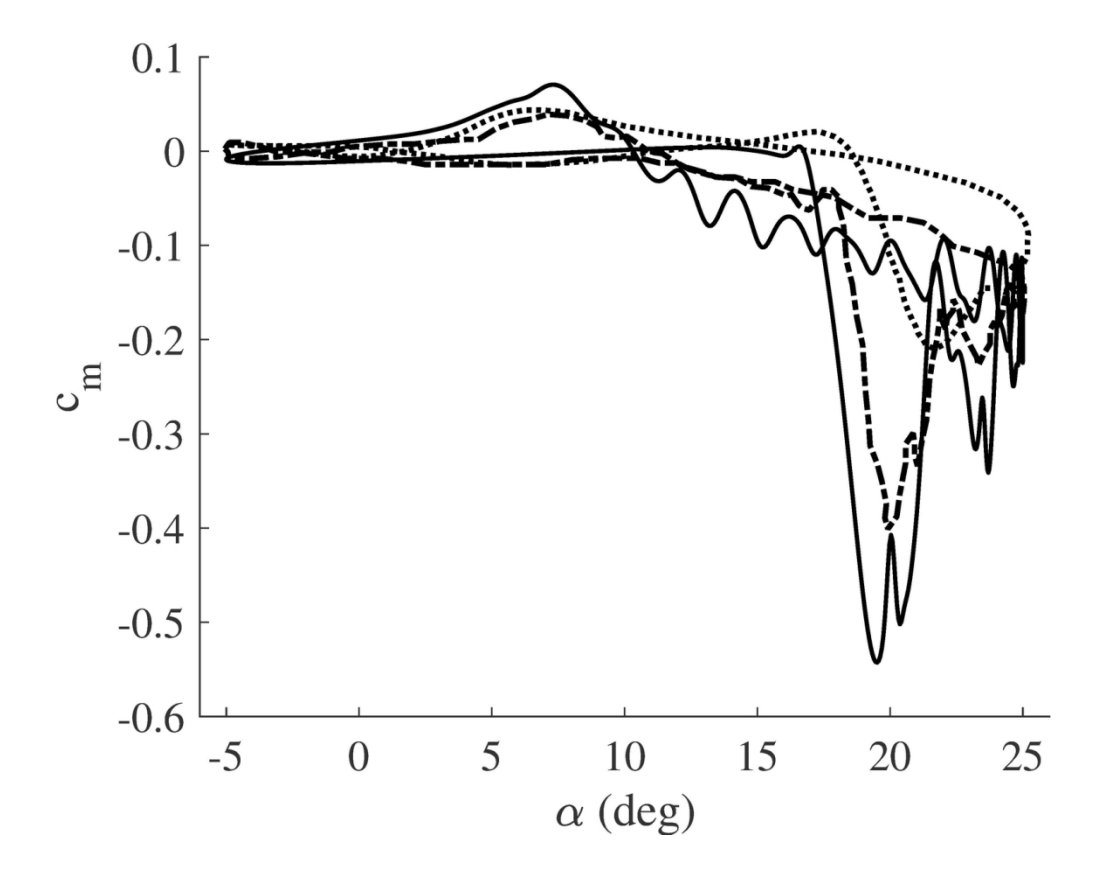
134x104mm (300 x 300 DPI)



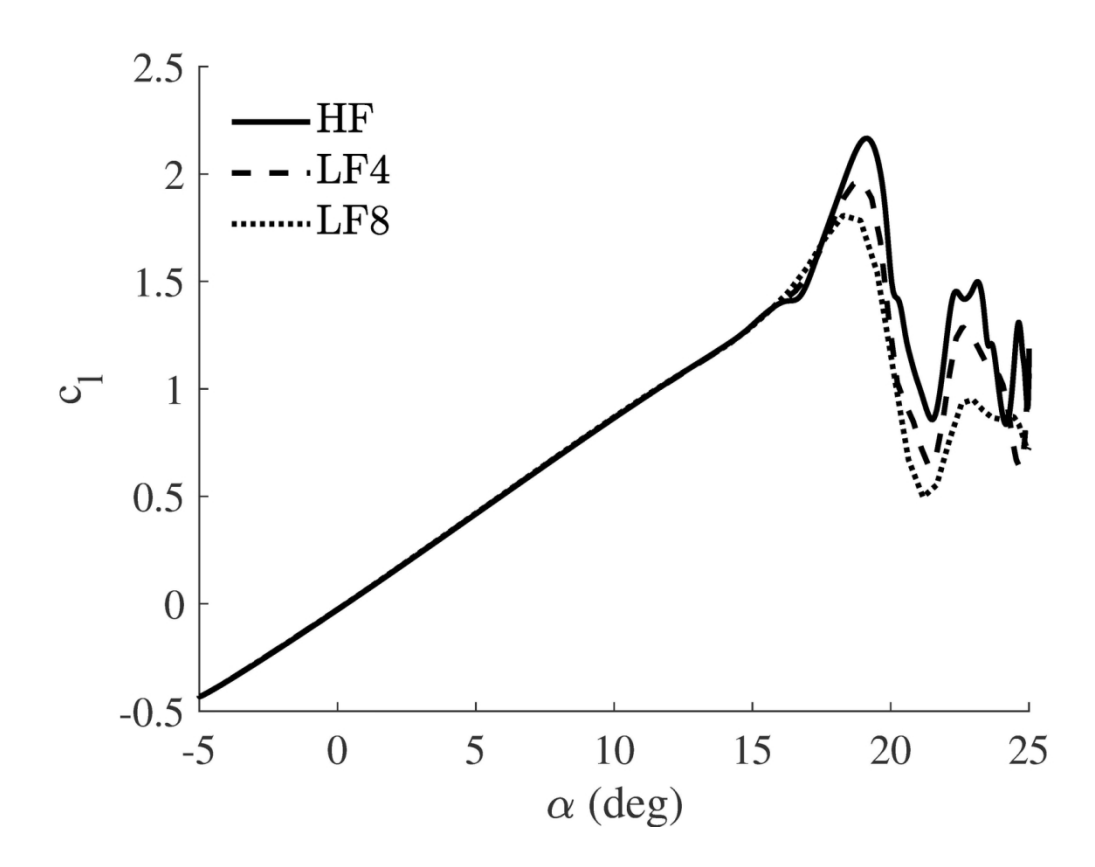
132x105mm (300 x 300 DPI)



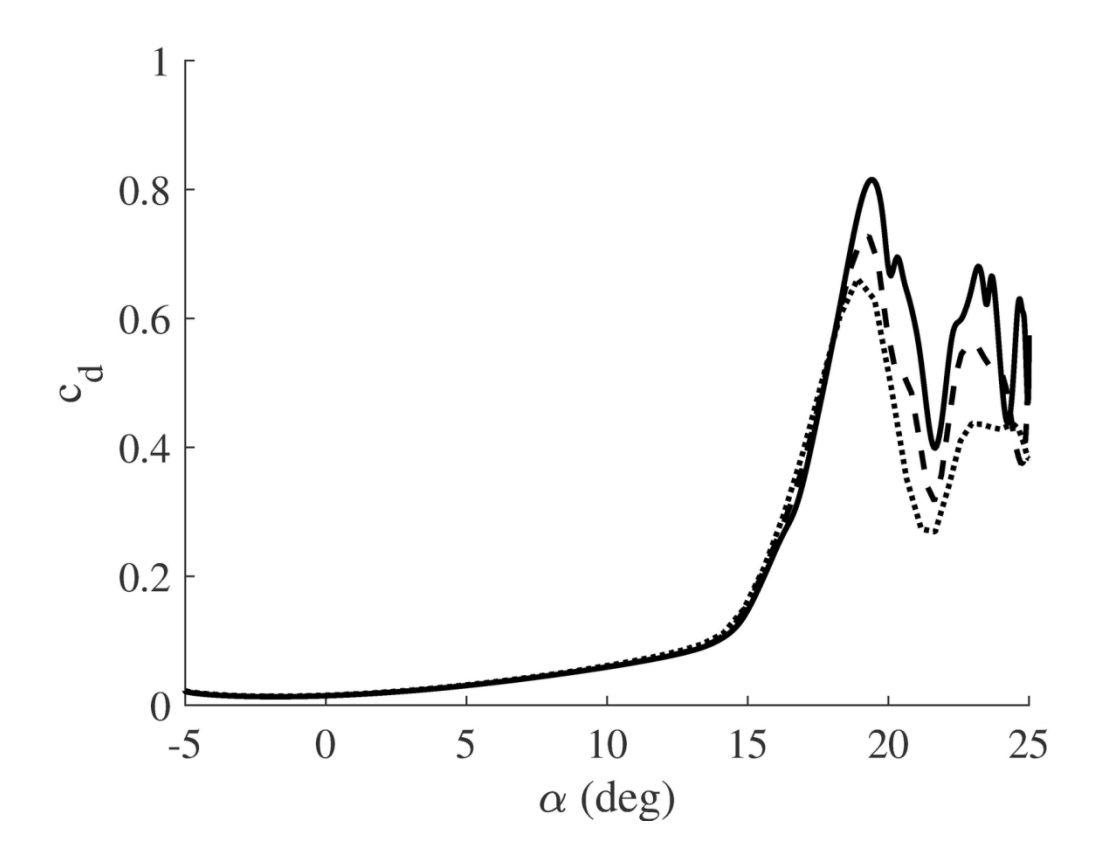
132x105mm (300 x 300 DPI)



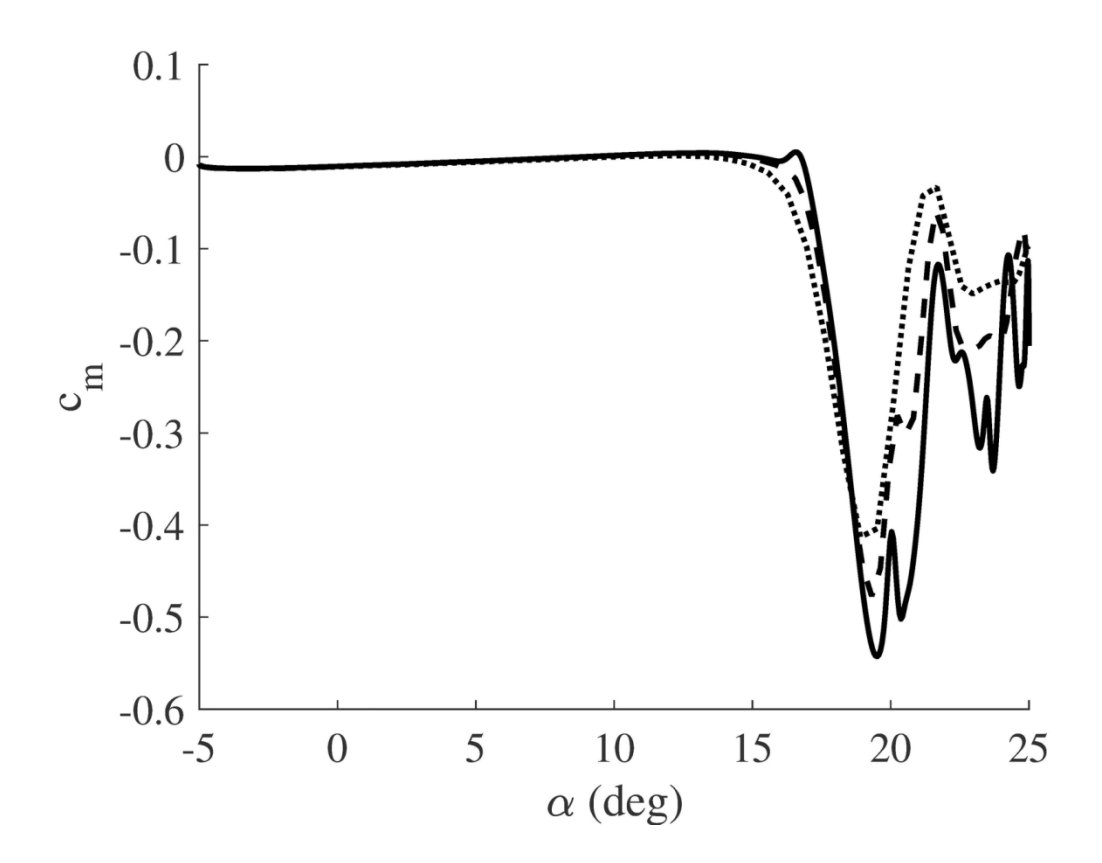
132x105mm (300 x 300 DPI)



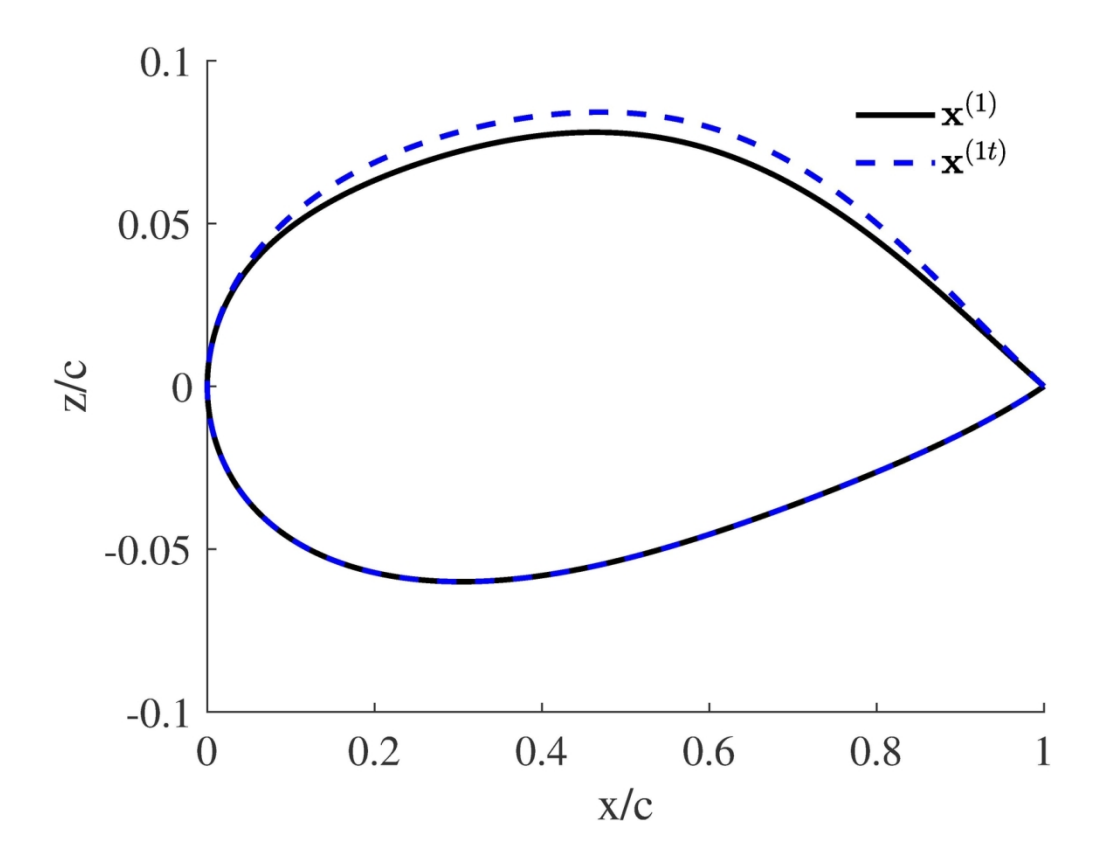
135x105mm (300 x 300 DPI)



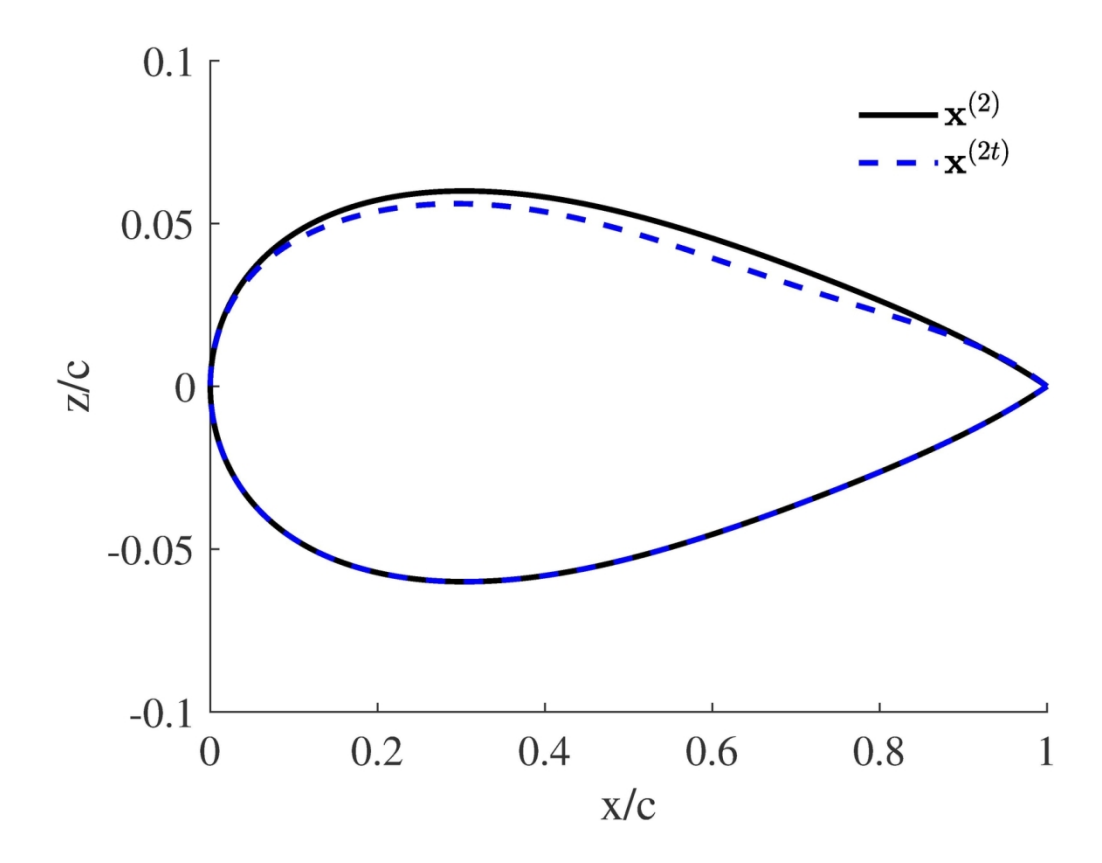
135x105mm (300 x 300 DPI)



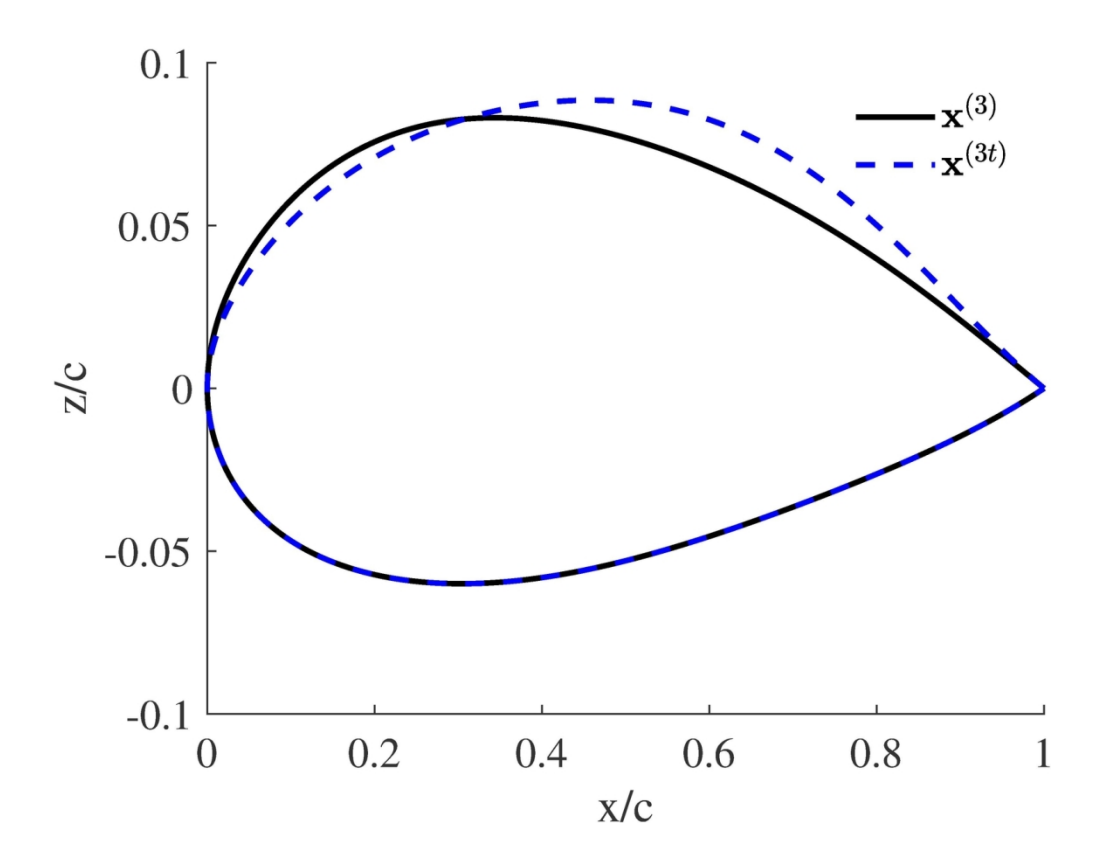
135x105mm (300 x 300 DPI)



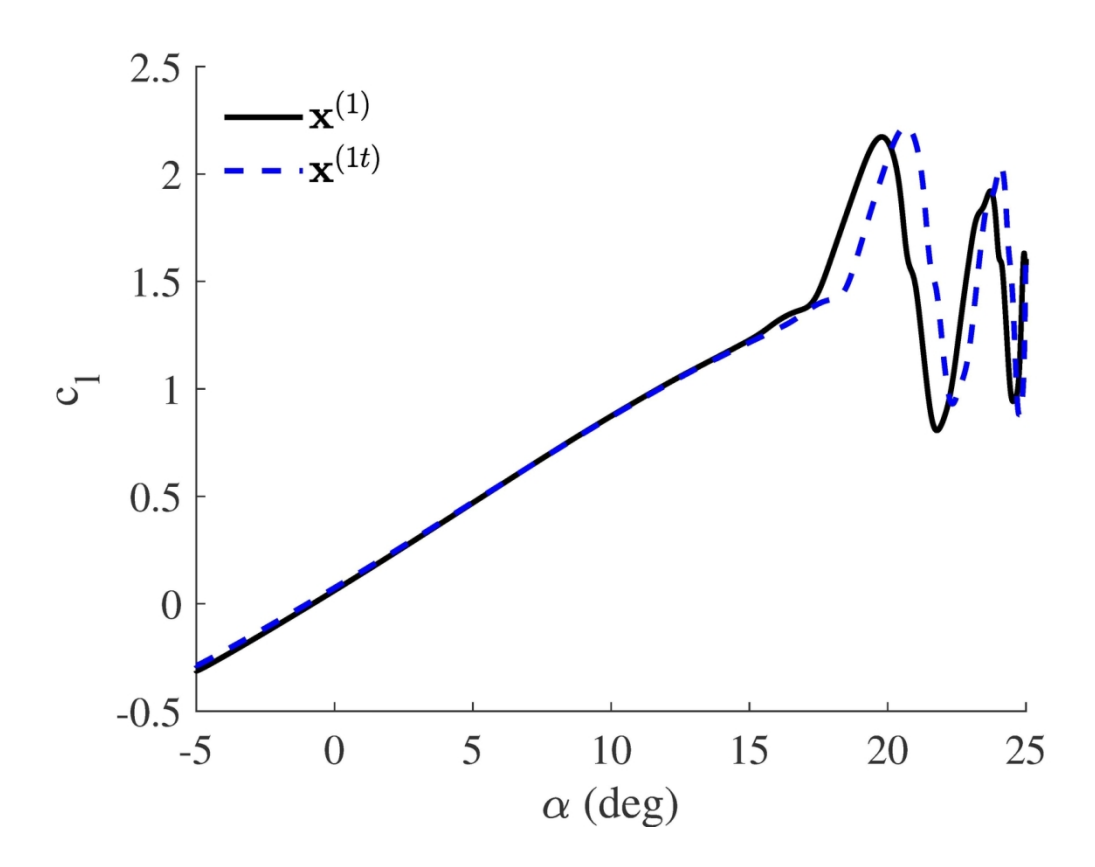
134x104mm (300 x 300 DPI)



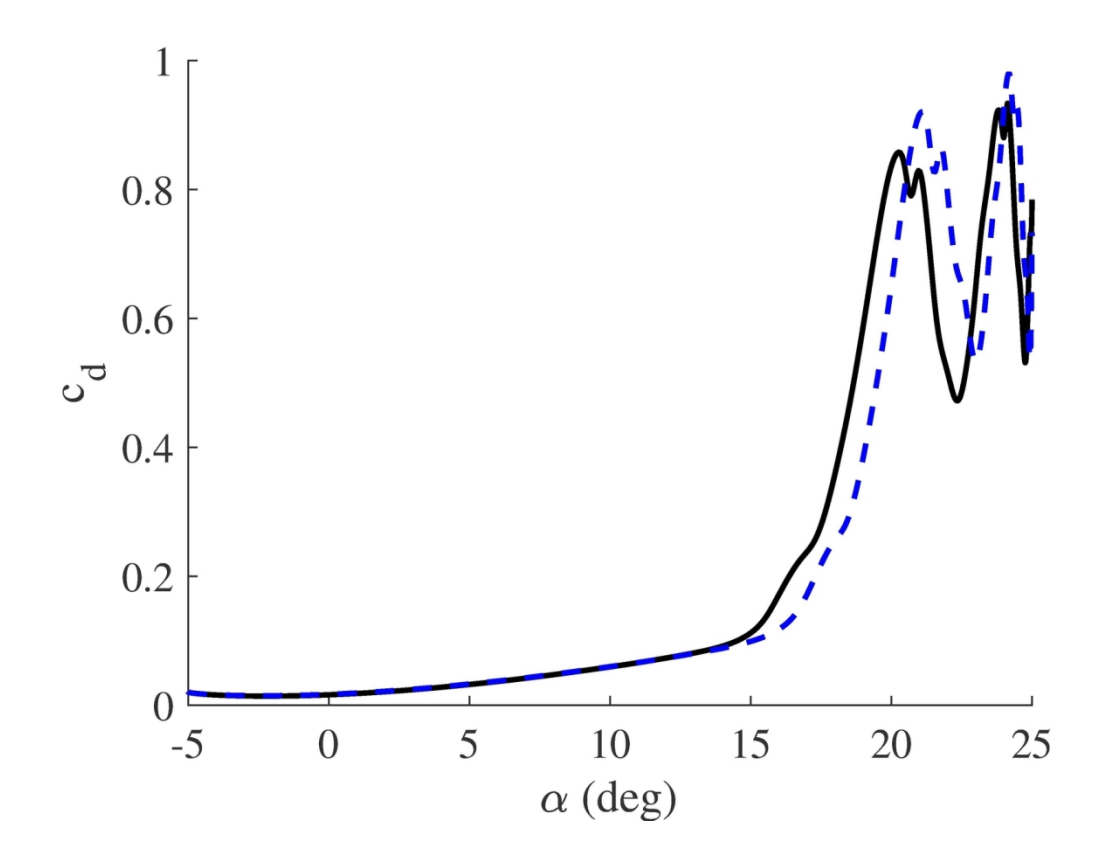
134x104mm (300 x 300 DPI)



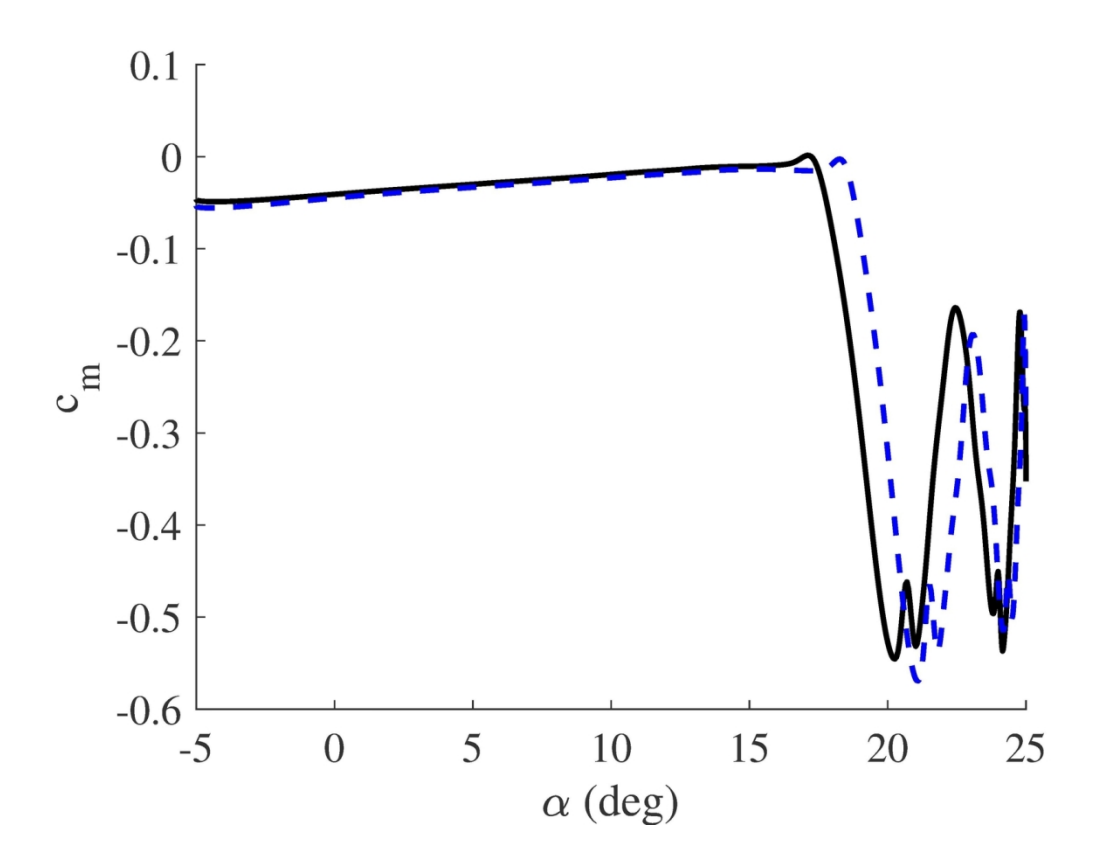
134x104mm (300 x 300 DPI)



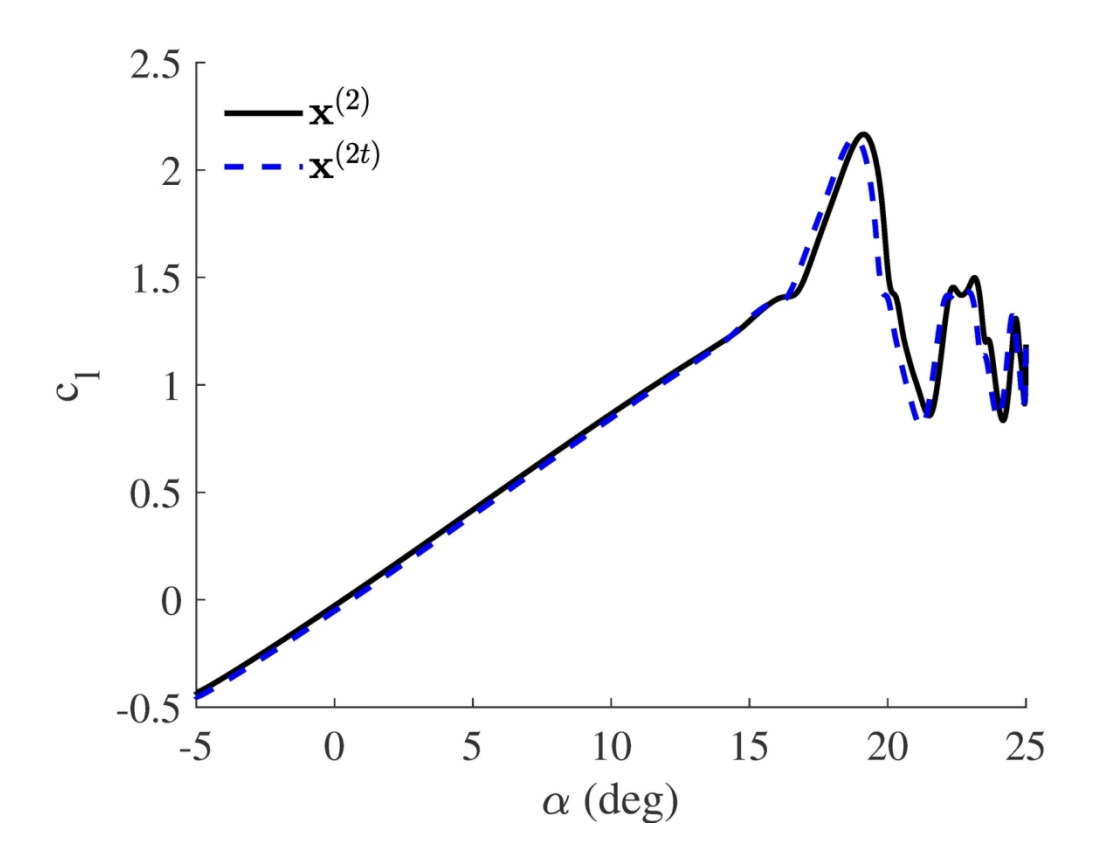
135x105mm (300 x 300 DPI)



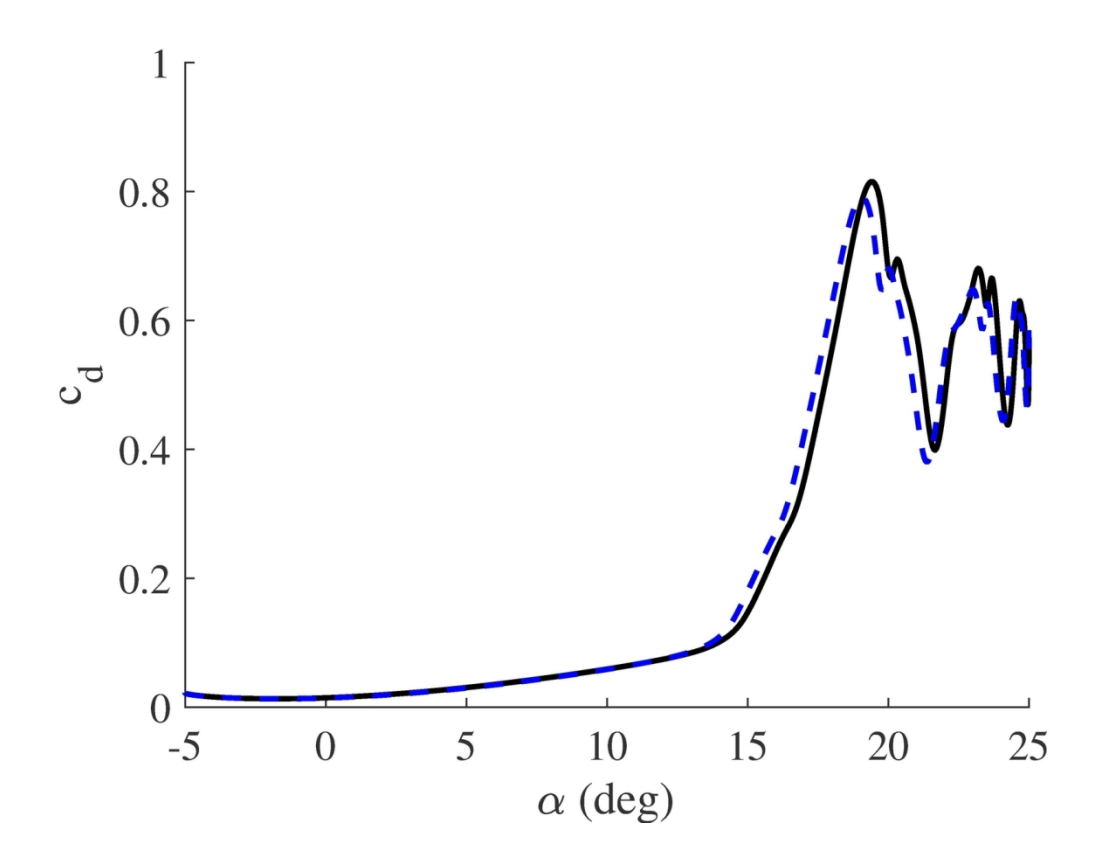
135x105mm (300 x 300 DPI)



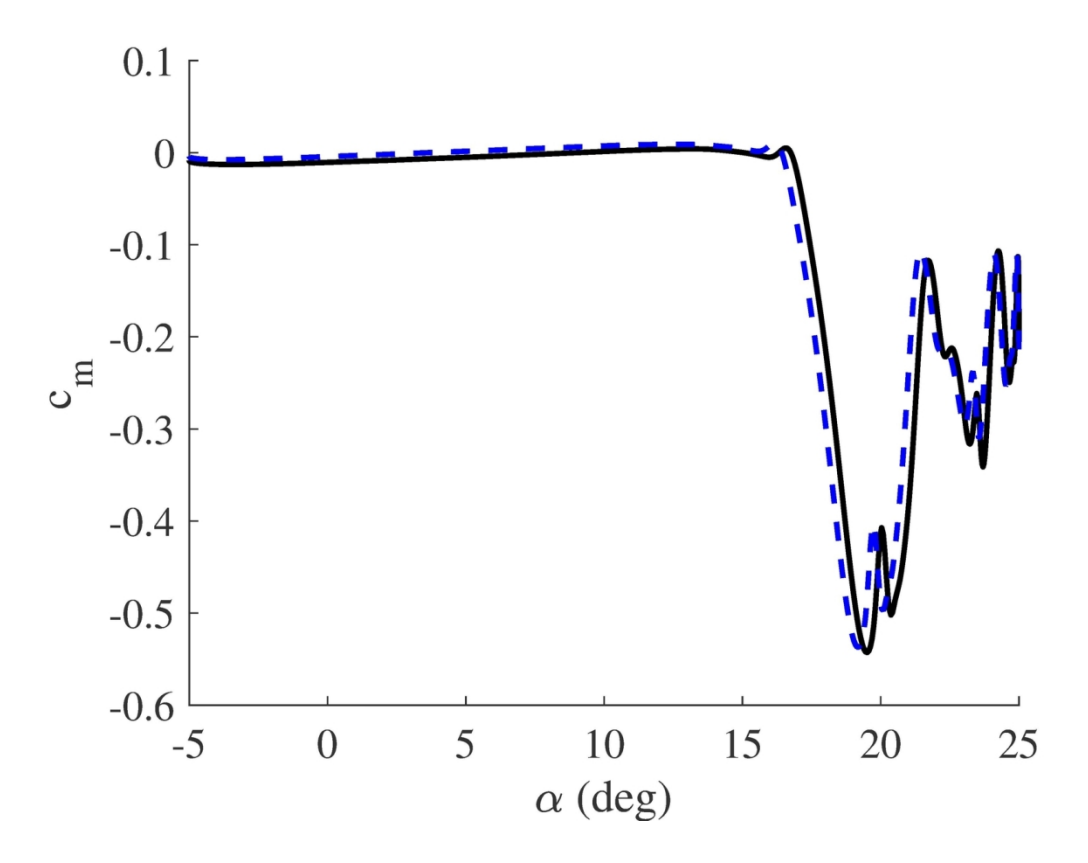
135x105mm (300 x 300 DPI)



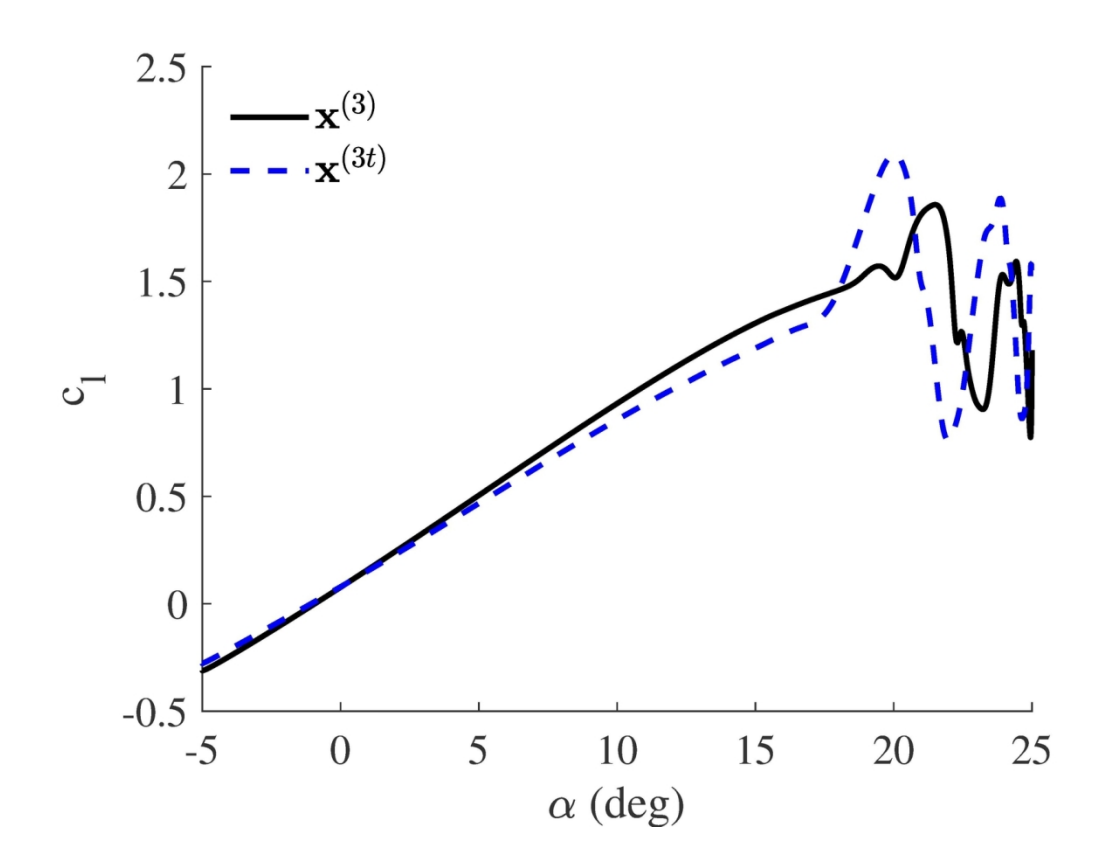
135x105mm (300 x 300 DPI)



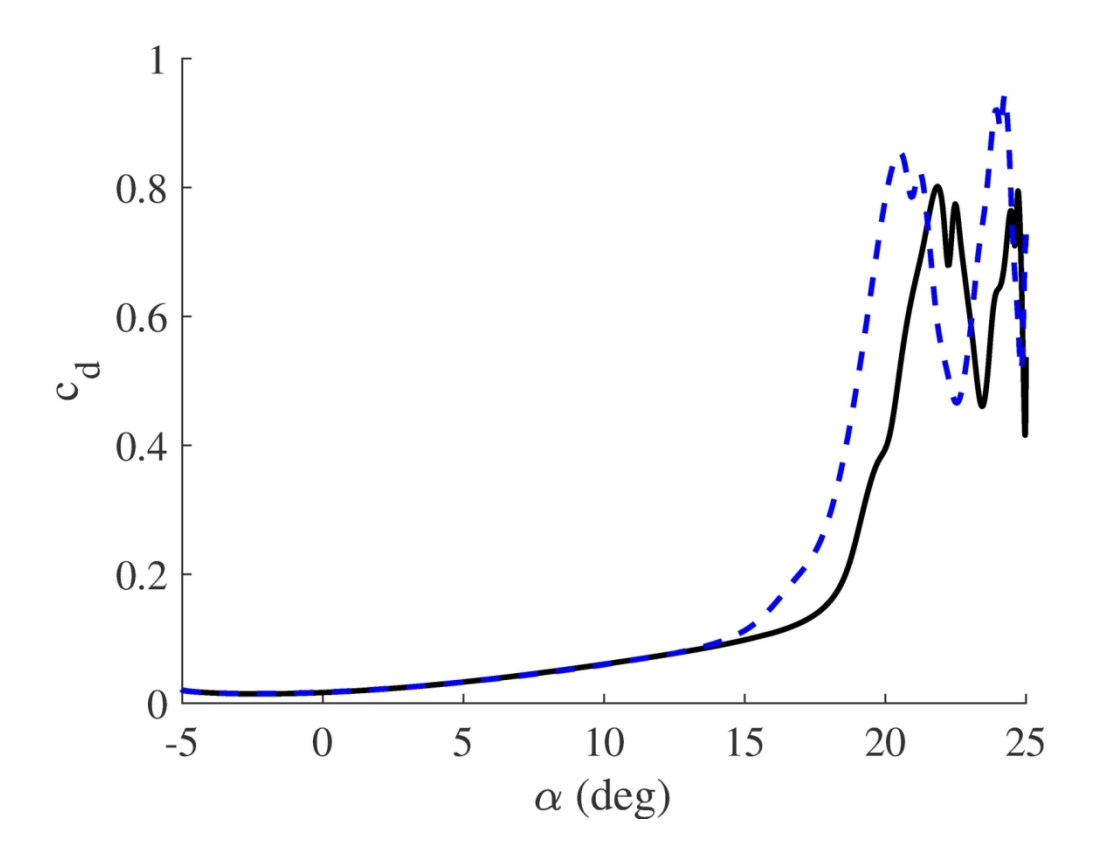
135x105mm (300 x 300 DPI)



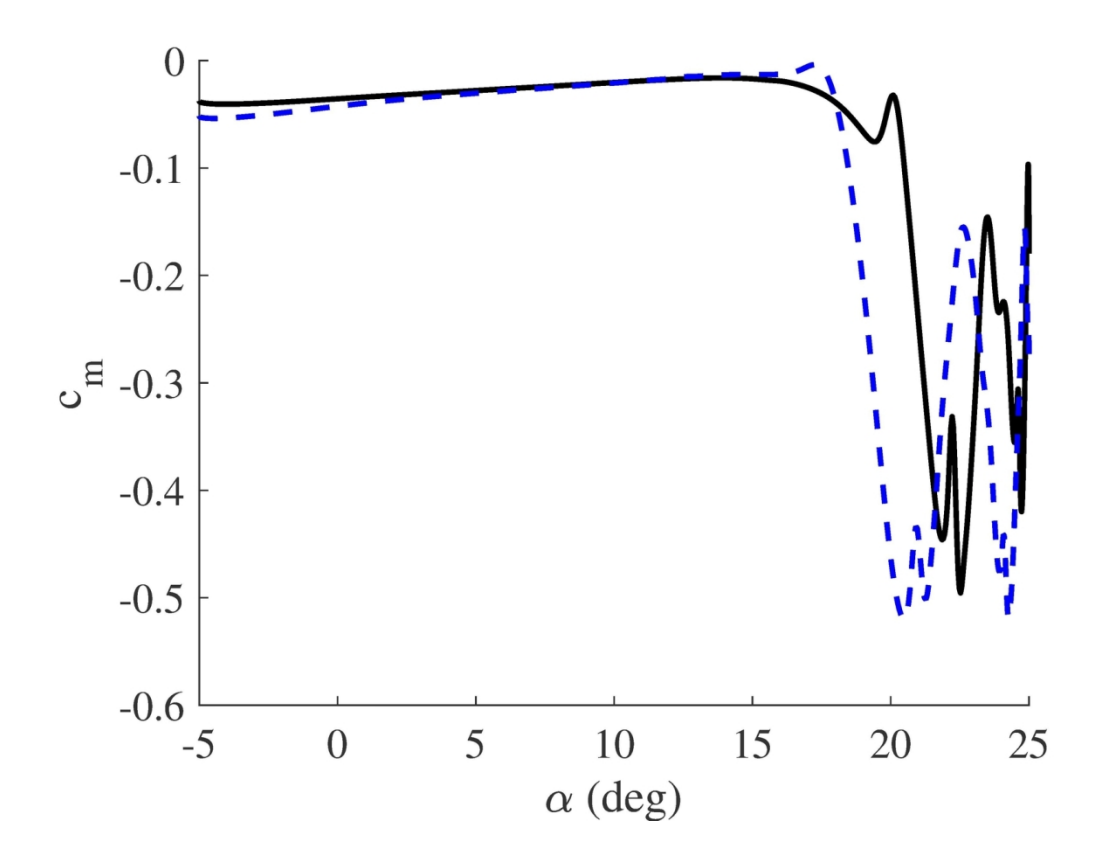
135x105mm (300 x 300 DPI)



135x105mm (300 x 300 DPI)



135x105mm (300 x 300 DPI)



135x105mm (300 x 300 DPI)